

Regimes of optical propagation through turbulence: theory and direct numerical simulations

Komal Kumari and Diego A. Donzis

Department of Aerospace Engineering, Texas A&M University, College Station, TX, USA

ABSTRACT

Classical work provides an analytical framework to predict distortions of an electromagnetic wave as it interacts with turbulence. However, there seems to be virtually no systematic validation of these predictions and assessment of the assumptions behind the theory. In this work, we present numerical results of optical distortions based on highly-resolved direct numerical simulations of turbulence at a range of conditions, and new theory which accounts for more realistic representations of turbulent fluctuations. This leads to a number of new results. First, we discover two new scaling regimes for the variance of phase and log-amplitude at propagations comparable to Kolmogorov scales. Second, our theory highlights and overcomes limitations of classical work including the effects of finite outer-scale, non-Kolmogorov intermittency corrections, and a more general representation of small scales. Third, we propose a new universal refractive-index structure parameter in terms of three non-dimensional parameters involving turbulence and optical scales. This yields a universal presentation of all scaling regimes in a new phase space. Finally, high-fidelity direct numerical simulations which resolve all turbulent scales are used to perform the first systematic assessment of classical and new scaling regimes. Excellent agreement is found between simulations and theoretical findings.

ARTICLE HISTORY


Received 9 December 2021
Accepted 21 November 2022

KEYWORDS

Turbulence; wave-front distortions; aero-optics; high-fidelity simulations

1. Introduction

The characteristics of electromagnetic waves are considerably affected when they propagate through a turbulent medium. For example, small variations in temperature or density lead to fluctuations in refractive index that in turn perturbs the phase and amplitude of the propagating wave [1, 2]. This optical turbulence can significantly distort the final wave front and result in degrading effects such as beam spreading, scintillation and jitter. Some of these effects can be characterized by optical path differences which has, thus, been studied extensively in different flows such as shear layers, wakes, and turbulent boundary layers [3–9]. These effects are also consequential in long-range laser communication systems [10]. Understanding these effects is important for fundamental and practical reasons. For example, if the characteristics of the turbulence are known, then one can predict, and thus

CONTACT Diego A. Donzis  donzis@tamu.edu

compensate for, the distortion of the wavefront. Conversely one can also use the information from the aberrated wave front to characterize both the medium and inhomogeneities encountered along the path.

Some of the early theoretical works to study the effect of turbulent fluctuations on the propagation of optical waves can be found in the monograph [2] by Tatarski. These are typically based on the classical work of Kolmogorov [11] to describe the statistical characteristic of turbulent fluctuations [2]. A detailed analysis of both amplitude and phase fluctuations using the method of smooth perturbations [2] shows that the way distortions grow as the traveled distance increases, depend upon the magnitude of the parameter $\sqrt{\lambda L}$ relative to turbulent length scales. Here λ is the optical wavelength and L is the propagation distance. At short distances, that is $\sqrt{\lambda L} \ll \eta$ where η is the so-called Kolmogorov scale, the amplitude fluctuations are independent of the optical wavelength and grow with distance as L^3 . This is also called the geometrical optics regime. In this regime, the correlation distance is of the order of η . At a comparatively larger distance, that is $\eta \ll \sqrt{\lambda L} \ll L_0$ where L_0 is the outer scale or the scale of largest turbulent fluctuations, the correlation distance is of the order of $\sqrt{\lambda L}$ and both phase and amplitude fluctuations now depend upon the optical wavelength. Tatarski's theory also assumes the outer-scale L_0 is infinite and thus, the variance of amplitude fluctuations grows indefinitely as $L^{11/6}$ with distance.

Numerical simulations to study the scaling of both phase and log-amplitude variance have relied extensively on the phase-screen approach [12–15]. In this methodology, the effect of turbulence is introduced using some form for the spectral distribution of fluctuations of phase. The final wavefront is computed as a net effect of series of phase screens applied to the vacuum propagation solution computed using the Fourier technique for solving the Fresnel integral [15, 16]. The log-amplitude variance then is typically compared against the results of the weak perturbation theory (or Rytov approximation) which yields an $L^{11/6}$ scaling for the log-amplitude variance [17–19]. This comparison is common in experimental work between the measured scintillation index and the Rytov approximation for so-called weak turbulence [20, 21]. For strong turbulence, the variance of the log-amplitude is found to saturate [22–24]. The distinction between weak and strong turbulence, however, is somewhat ambiguous and is usually based on the Rytov parameter or the structure function parameter exceeding some threshold. Furthermore, there is no systematic validation of the different scaling regimes from either simulations or experiments. In some of the early experimental work by Gracheva and Gurvich [17], the variance was measured at five propagation distances and despite significant scatter, it was concluded that the log-amplitude variance scales as $\sim L^{1.6}$ which is close to, though still different from $L^{11/6} \approx L^{1.83}$. At shorter distances, it has been noted [17] that measurements are significantly affected by sensor noise. This presents challenges in obtaining accurate measurements in the geometrical optics regime in the experiments.

Although the theory has not been systematically validated in all regimes, one can still use some of its implications to obtain, for example, turbulent characteristics. This has been suggested in [25] where scintillation index measurements were performed at two distances, one in geometrical optical regime and another one in the $L^{11/6}$ regime. Since the log-amplitude variance also depends upon the inner scale of turbulence in the geometrical optics regime, it can be estimated without measuring the structure function parameter (C_n^2) independently. This is helpful since in most experiments the distance might not be sufficiently large to observe the $L^{11/6}$ regime, even though $L^{11/6}$ results have nonetheless been

used to compute C_n^2 . This concern has also been raised in [26] where it was also shown that the bump in the spectrum of temperature (or consequently refractive index) spectrum can further amplify the optical scintillations and push the transition to the $L^{11/6}$ to larger distances [27]. An accurate determination of transition distances (and thus the regime for the propagation) is therefore critical to understand experimental and numerical results as well as to accurately determine important aero-optics parameters from measurements.

In this work, we revisit the classical theory of Tatarski for the propagation of plane electromagnetic waves through turbulence. Specifically, we relax some of the assumptions in this classical theory and derive new scaling regimes at short distances for both amplitude and phase fluctuations. By including the effect of finite outer scale, we also compute closed-form expressions for variance of phase fluctuations, a result previously unknown. Different scaling regimes and the transition between them is summarized in a phase map in terms of appropriate non-dimensional parameters. The effect of non-Kolmogorov turbulence with intermittency correction in the inertial range and non-Gaussian roll-off in the dissipation range is also investigated. The theoretical work is supplemented with highly resolved numerical simulations of the paraxial equation with density fluctuations from some of the best resolved direct numerical simulations of the compressible Navier–Stokes equations. These simulations clearly exhibit different scaling regimes for log-amplitude variance close to the corresponding theoretical values. To the authors' knowledge, this is the first systematic study that assesses all the theoretical scaling regimes.

The rest of this paper is organized as follows. We begin with an overview of Tatarski's theory in Section 2, followed by the generalization of this classical work in Section 3. In Section 4, we present the transition between the scaling regimes for log-amplitude and phase variance. The non-dimensionalization of different scaling regimes and the transitions therein is performed in Section 5. Results from numerical simulations are discussed in Section 6. Lastly, the discussions and concluding remarks are presented in Section 7.

2. Overview of Tatarski's theory

The well-known Maxwell vector equations describe the propagation of electromagnetic waves through a medium that may exhibit fluctuations in the refractive index. If $\lambda \ll \eta$, where λ is the optical wavelength and η is the length scale of turbulent fluctuations, then one can show that the vector equations take a simplified scalar form

$$(\nabla + \kappa^2)E = -2\kappa^2 n'E. \quad (1)$$

Here E can be any component of electric or magnetic field vector. In Equation (1), $\kappa = 2\pi/\lambda$ is the optical wavenumber and n' denotes fluctuations in the refractive index field which are related to the density fluctuations through $n = 1 + K_{GD}(\lambda)\rho$, where K_{GD} is the Gladstone–Dale constant and ρ is the density [28, 29]. We consider the effect of refractive index fluctuations on a plane wave of the form $E_0 = A_0 e^{iS_0}$, where $S_0 = \kappa \mathbf{x}$ is the initial phase and A_0 is the initial amplitude. If the distorted wave is represented as $E = Ae^{iS}$, with S and A being the phase and amplitude respectively at some distance from the source, we can define a new variable as $\psi = \log A + iS$. Its fluctuating part would then be given by $\psi' = \psi - \psi_0 = \log(A/A_0) + i(S - S_0)$, where $\psi_0 = \log A_0 + iS_0$ corresponds to the initial plane wave at the source. The real and imaginary parts of ψ' are denoted by $\chi' =$

$\Re(\psi') = \log(A/A_0)$ and $S' = \Im(\psi') = S - S_0$, respectively. They describe the fluctuations in log-amplitude and phase of a plane electromagnetic wave. On substituting $E = e^{\psi_0 + \psi}$ in Equation (1) and linearizing the resulting equation, we obtain $\nabla\psi' + 2i\kappa\Delta\psi' = -2\kappa^2 n'$ or its paraxial approximation,

$$\frac{\partial^2\psi'}{\partial y^2} + \frac{\partial^2\psi'}{\partial z^2} + 2i\kappa\frac{\partial\psi'}{\partial x} = -2\kappa^2 n' \quad (2)$$

when the term $\partial^2\psi'/\partial x^2$ in the direction of propagation is neglected. Here the fluid is non-conducting and the timescale of optical propagation is negligible in comparison to the flow time scales. Thus the fluctuations in electromagnetic field do not alter the underlying turbulent field. Combining Equation (2) with the definition of ψ' and separating the real and imaginary parts yields an equation for χ' and another one for S' . Following the notation and simplifications described in [30], one can solve the resulting PDEs to obtain:

$$F_{\chi\chi}^{(2)}(k) \approx \kappa^2 L \int_0^L \left(1 - \frac{\kappa}{k^2 L} \sin \frac{k^2 L}{\kappa} - \frac{\xi}{2L} \left(1 - \cos \frac{k^2 L}{\kappa} \right) \right) F_{nn}^{(2)}(k, \xi) d\xi. \quad (3)$$

Equation (3) relates $F_{\chi\chi}^{(2)}(k)$, the two-dimensional spectrum (in the plane $x = L$) of χ' with $F_{nn}^{(2)}(k, \xi)$, the Fourier transform of the three-dimensional two-point correlation in the plane perpendicular to the propagation with ξ being the distance (in x) between the two points [2]. In the above expression $k = \sqrt{k_2^2 + k_3^2}$. A similar relation can also be obtained between $F_{nn}^{(2)}(k, \xi)$ and the two-dimensional spectrum of phase $F_{SS}^{(2)}(k)$ in the plane $x = L$.

If we only consider high wavenumbers relative to the propagation, that is

$$1/k \ll L, \quad (4)$$

or $\xi \ll L$ in the region where $F_{nn}^{(2)}(k, \xi)$ is non-zero, then the second term in Equation (3) can be neglected. Since $F_{nn}^{(2)}(k, \xi)$ is negligibly small for $\xi > 1/k$, the resulting integral can be evaluated over the range $0 \leq \xi < \infty$ without much error. For locally isotropic turbulence, one can also write the two-dimensional spectral density of the refractive index in Equation (3) in terms of its three-dimensional counterpart $F_{nn}^{(2)}(k, \xi)$:

$$F_{nn}^{(2)}(k, \xi) = \int_{-\infty}^{\infty} \cos(k_1 \xi) F_{nn} \left(\sqrt{k_1^2 + k^2} \right) dk_1, \quad \text{or} \quad \int_0^{\infty} F_{nn}^{(2)}(k, \xi) d\xi = \pi F_{nn}(k). \quad (5)$$

Taken together, these simplifications yield

$$F_{\chi\chi}^{(2)}(k) = \pi \kappa^2 L \left(1 - \frac{\kappa}{k^2 L} \sin \frac{k^2 L}{\kappa} \right) F_{nn}(k). \quad (6)$$

An important length scale that appears in Equation (6) is $\sqrt{L/\kappa}$ (or $\sqrt{\lambda L}$) which is the radius of the first Fresnel zone. When $\sqrt{\lambda L} \ll \eta$, where η is the Kolmogorov scale, Equation (6) simplifies to:

$$F_{\chi\chi}^{(2)}(k) = \frac{1}{6} \pi L^3 k^4 F_{nn}(k), \quad (7)$$

which implies that the log-amplitude fluctuations are independent of the optical wavelength. This is also the so-called geometric optics regime in which eddies of order η have the strongest influence on the log-amplitude fluctuations. On the other hand, when the parameter $\sqrt{\lambda L}$ is in the inertial range of scales of the turbulence, i.e. $\eta \ll \sqrt{\lambda L} \ll L_0$, with L_0 being the largest (or outer) scale, the largest contribution to the log-amplitude fluctuations come for refractive index inhomogeneities of the order $\sqrt{\lambda L}$. In this case, the statistics of the log-amplitude fluctuations are given by the full expression in Equation (6). At much larger distances such that $\sqrt{\lambda L} \gg L_0$, we have

$$F_{\chi\chi}^{(2)}(k) \approx \pi L k^2 F_{nn}(k), \quad (8)$$

when $k > 2\pi/L_0$.

In all these cases, the variance of log-amplitude fluctuations can be readily computed as

$$\overline{\chi'^2} = 2\pi \int_0^\infty F_{\chi\chi}^{(2)}(k) k dk. \quad (9)$$

Based on the Kolmogorov theory of turbulence, the refractive index fluctuations possess a spectral distribution of the form $F_{nn}(k) = \frac{C_n^2}{4\pi} k^{-11/3} \exp(-\alpha \eta^2 k^2)$ [30]. This spectral density is associated with the structure function of refractive index field that follows the classical Kolmogorov two-thirds law, i.e. $D_n(d) = C_n^2 d^{2/3}$, in the inertial range. Here C_n^2 is the so-called structure function parameter. Following simplifications described in great detail in [2], two distinct scaling laws with propagation distance L are obtained for the variance of log-amplitude fluctuations,

$$\overline{\chi'^2} = C_n^2 \begin{cases} \frac{\pi}{144} \Gamma\left(\frac{1}{6}\right) \alpha^{-7/6} \eta^{-7/3} L^3, & \sqrt{\lambda L} \ll \eta \\ \frac{9\pi}{55} \Gamma\left(\frac{1}{6}\right) \sin \frac{11\pi}{12} \kappa^{7/6} L^{11/6}, & \eta \ll \sqrt{\lambda L} \ll L_0 \end{cases} \quad (10)$$

Here $\Gamma(\cdot)$ is the gamma function. While these theoretical results have been known for several decades, there are virtually no comprehensive systematic studies (experimental or simulations) that verify these scaling laws. In an early experimental work, [17] observed a $L^{1.6}$ scaling for the variance of log-amplitude fluctuations instead of $L^{11/6} \approx L^{1.83}$. A number of subsequent experiments compared the measured values of $\overline{\chi'^2}$ against the so-called Rytov index ($\overline{\chi_R'^2} \propto C_n^2 \kappa^{7/6} L^{11/6}$). Generally the data show a near linear scaling giving support to the second expression in Equation (10), at least for $\overline{\chi_R'^2} < 1$. For larger values of $\overline{\chi_R'^2} \gtrsim 1$, the experimental $\overline{\chi'^2}$ tends to saturate, a phenomenon that has also been theoretically investigated in numerous studies [22–24, 31]. The L^3 regime has received even less attention in the literature, though some recent experimental work in carefully designed laboratory setups appear to confirm some of these findings [32]. Yet, simulations or experiments that explicitly show both L^3 and $L^{11/6}$ scalings for variance of log-amplitude variance at a range of conditions are practically non-existent. We address this gap in theory and simulations in this work.

Before we present data from well-resolved direct numerical simulations, we derive new scaling laws for the fluctuations in log-amplitude and phase at very short distances. These are regimes that are not included in classical theoretical work [2] or in other subsequent

studies. We also generalize the theoretical work of Tatarski to include the effect of non-Kolmogorov turbulence in the inertial range and non-Gaussian roll-off in the dissipation range. The different scaling regimes for variance of log-amplitude are summarized in a phase map obtained in terms of relevant non-dimensional parameters that will be useful for guiding experiments and simulations.

3. Generalization of Tatarski's theory

3.1. Scaling at short propagation distance

In the theoretical developments in [2] (also summarized in Section 2), it was assumed that only the scales of refractive index fluctuations that satisfy $1/k \ll L$ (Equation 4) significantly contribute to the corresponding variances. At very short distances, however, since a very small region comprising only high wavenumbers in the refractive index spectrum satisfy $1/k \ll L$, the variance in log-amplitude or phase fluctuations so computed is not accurate. Mathematically, this implies that the term $\frac{\xi}{2L} (1 - \cos \frac{k^2 L}{\kappa})$ in Equation (3) cannot be neglected at short distances. Thus, when the propagation distance is of the order of the Kolmogorov scale η , the results summarized in Section 2 (or [2, 30]) are no longer adequate as we show next.

We start our analysis by substituting $F_{nn}^{(2)}(k, \xi)$ from Equation (5) in Equation (3) to write the two-dimensional spectral density as

$$F_{\chi\chi}^{(2)}(k) \approx \kappa^2 L \int_0^L \left\{ 1 - \frac{\kappa}{k^2 L} \sin \frac{k^2 L}{\kappa} - \frac{\xi}{2L} \left(1 - \cos \frac{k^2 L}{\kappa} \right) \right\} \left(\int_{-\infty}^{\infty} \cos(k_1 \xi) F_{nn} \left(\sqrt{k_1^2 + k^2} \right) dk_1 \right) d\xi, \quad (11)$$

which involves integrals with respect to ξ and k_1 . On integrating Equation (11) with respect to ξ with $F_{nn}(k) = \frac{C_n^2}{4\pi} k^{-11/3} \exp(-\alpha \eta^2 k^2)$, we obtain

$$F_{\chi\chi}^{(2)}(k) \approx C_n^2 \kappa^2 \int_{-\infty}^{\infty} \left\{ \frac{e^{-\alpha \eta^2 (k^2 + k_1^2)} \left(k_1 \sin(k_1 L) \left(k^2 L \left(\cos \frac{k^2 L}{\kappa} + 1 \right) - 2\kappa \sin \frac{k^2 L}{\kappa} \right) - 2k^2 (\cos(k_1 L) - 1) \sin^2 \frac{k^2 L}{2\kappa} \right)}{8\pi k^2 k_1^2 (k^2 + k_1^2)^{11/6}} \right\} dk_1, \quad (12)$$

Since we are only interested in the characterization of $\overline{\chi^2}$ at very short distances, we can take a Taylor series expansion of Equation (12) about $L = 0$ and retain only the leading order term,

$$F_{\chi\chi}^{(2)}(k) \approx C_n^2 \int_{-\infty}^{\infty} \frac{k^4 e^{-\alpha \eta^2 (k^2 + k_1^2)}}{96\pi (k^2 + k_1^2)^{11/6}} L^4 dk_1. \quad (13)$$

We note that similar to Equation (7) in the geometrical optics regime, the above expression is independent of the optical wavelength. Following integration with respect to k_1 ,

the variance $\overline{\chi'^2}$ is computed from Equation (9) and is equal to

$$\overline{\chi'^2} = C_n^2 \frac{1}{90} \Gamma\left(\frac{5}{3}\right) \alpha^{-5/3} \eta^{-10/3} L^4. \quad (14)$$

Thus, at very short propagation distances, the log-amplitude variance grows steeply as L^4 . This new L^4 scaling has not been reported in any of the previous theoretical, experimental, or numerical works. If experimental measurements can be made at distances at which Equation (14) is valid, the expression in $\overline{\chi'^2}$ can be utilized to compute important turbulence parameters such as α and η . In Section 6, we verify this new L^4 scaling using high-fidelity direct numerical simulations at varying turbulent conditions.

Another simplifying assumption made in classical analyses is that the outer scale (L_0) or the largest scales of refractive index fluctuations are infinitely large, that is, $L_0 \rightarrow \infty$. The effect of finite outer scale can be incorporated in the limits of the integral in Equation (9) as

$$\overline{\chi'^2} = 2\pi \int_{1/L_0}^{\infty} F_{\chi\chi}^{(2)}(k) k dk. \quad (15)$$

At very short distances (formally $L \rightarrow 0$), substituting Equation (12) in Equation (15) yields

$$\begin{aligned} \overline{\chi'^2} = C_n^2 \left\{ \frac{4\Gamma\left(-\frac{4}{3}\right) {}_1F_1\left(-\frac{5}{2}; -\frac{2}{3}; -\frac{\alpha\eta^2}{L_0^2}\right)}{1215\alpha^{5/3}\eta^{10/3}} - \frac{\sqrt[3]{\alpha}\eta^{2/3}\Gamma\left(-\frac{4}{3}\right) {}_1F_1\left(-\frac{1}{2}; \frac{4}{3}; -\frac{\alpha\eta^2}{L_0^2}\right)}{36L_0^4} \right. \\ \left. + \frac{\Gamma\left(-\frac{4}{3}\right) {}_1F_1\left(-\frac{3}{2}; \frac{1}{3}; -\frac{\alpha\eta^2}{L_0^2}\right)}{81\alpha^{2/3}\eta^{4/3}L_0^2} - \frac{\pi^{3/2} {}_2F_2\left(-\frac{5}{6}, \frac{5}{3}; -\frac{1}{3}, \frac{8}{3}; -\frac{\alpha\eta^2}{L_0^2}\right)}{216\sqrt{3}L_0^{10/3}\Gamma\left(\frac{11}{6}\right)\Gamma\left(\frac{8}{3}\right)} \right\} L^4, \quad (16) \end{aligned}$$

where ${}_1F_1$ is a Kummer confluent hypergeometric function and ${}_2F_2$ is a generalized hypergeometric function [33, 34]. Equation (16) reduces to Equation (14) when $L_0 \rightarrow \infty$ implying that the effects of outer-scale are weak at such short distances and relevant only at low Reynolds number. Similar expressions can also be derived for the L^3 and $L^{11/6}$ regimes. This is done next.

3.2. Non-Kolmogorov turbulence

It has been known for a long time that realistic turbulence does not behave in all the details as predicted by Kolmogorov 11 theory [11], a fact recognized by Kolmogorov himself which led to his refined similarity hypothesis [35]. One of the limitations is the phenomenon of intermittency [36], the tendency for turbulence to develop very large fluctuations that are also very localized in space and time. A number of models and theories have been developed since then to account for its effects [37], one of which is a correction to the famous 5/3 slope for the energy spectrum. Intermittency, being a small-scale effect, also has a large influence at high wavenumbers, specifically in the dissipative range [38]. We, thus, generalize the model spectrum representing turbulence by including intermittency corrections to inertial-range scaling and the specific form of exponential roll-off at high wavenumbers.

For this we consider

$$F_{nn}(k) = \frac{C_n^2}{4\pi} k^{-\frac{11}{3}} (k\eta)^{-\frac{r}{2}} \exp(-\alpha(\eta k)^\gamma), \quad (17)$$

where r is the so-called intermittency correction in the inertial range [36]. The effect of a similar correction r in the context of optical distortions has been investigated in [39–41]. The dissipation range parameter γ in Equation (17) is traditionally assumed to be 2 [2]. In recent work, this issue has been examined and it was shown that while there appear to be two regimes in the dissipation range with different values of γ [38, 42], for very high wavenumbers γ may not be too far from unity. Note, however, that Equation (17) refers to the index of refraction spectrum which, in our work, is solely linked to density fluctuations. As shown in [43], for small fluctuations, temperature behaves, to a good approximation, as a passive scalar [44]. Furthermore, in these circumstances, one can also reliably use an isentropic relation to show that density fluctuations can also, then, be treated as a passive scalar [45]. For passive scalars, it has been shown [46] that the exponential roll-off in the spectrum at high wavenumbers agrees with $\gamma = 1$ as suggested by Kraichnan [47, 48] instead of the earlier suggestion $\gamma = 2$ by Batchelor [49] even for Prandtl numbers of order 1 as in air and those flows considered here. Physically, this is an important consideration since $\gamma = 2$ implies much faster decay of refractive index fluctuation at the small scales which can produce, thus, less significant optical distortions. In fact, as we will show in Section 4, this could have a first-order effect on the location of the transitions between propagation regimes for log-amplitude variations, for example. We note that for solenoidally forced compressible turbulence, the density field behaves as a passive scalar [43, 45] which approximately follows the model spectrum from Equation (17). For compressible turbulence dominated by dilatational motions, however, the existence of classical cascades and their consequences including the applicability of Equation (17) or its generalizations is still an open question [50–52]. Nevertheless, we find from DNS that Equation (17) is still a reasonable representation of density spectrum for all conditions presented here by choosing the parameters (r, γ, α) judiciously. This is the approach adopted here.

Whenever possible, we obtain analytical expressions for arbitrary values of γ in Equation (17). If not possible, we will instead focus on the two values discussed above (i.e. 1 and 2). We also derive these scaling laws with finite L_0 wherever possible in Equation (15) to compute $\overline{\chi'^2}$.

We finally note that in order for the problem to remain tractable from a theoretical perspective we do not include other effects such as anisotropy and the bottleneck effect. The former has been studied in the literature [39, 53] and results seem to indicate that the effects of anisotropy are confined to prefactors in the expressions for variances such as those presented here. If this is indeed the case, then scaling exponents may be unaffected by anisotropy effects. Another effect not captured in Equation (17) is the so-called bottleneck effect which appears in incompressible and compressible flows [43, 54]. This small change in the spectrum at the bottom of the inertial range has been shown to be responsible for small changes in the variance of log-amplitude around the transition from L^3 to $L^{11/6}$, though the asymptotic behavior in both regimes is identical to those obtained without the bottleneck [27]. A more formal study of these two effects will be presented somewhere else.

3.2.1. L^4 regime

We start by generalizing the results for very short propagation distances, that is in the limit $L \rightarrow 0$. For this we take the general expression Equation (11) with $F_{nn}(k)$ from Equation (17). As before, we compute the integral with respect to ξ and take the leading order term of the Taylor series expansion of the resulting expression in L about zero. This yields an expression for $F_{\chi\chi}^{(2)}(k)$ similar to Equation (13) with an integral in k_1 . To obtain a closed-form expression, it is convenient to substitute $F_{\chi\chi}^{(2)}(k)$ into Equation (15), integrate in k first, take the limit $L_0 \rightarrow \infty$, and finally integrating in k_1 to obtain, for $\gamma = 1$ and 2,

$$\overline{\chi^2} = C_n^2 \begin{cases} \frac{1}{45} \alpha^{\frac{r}{2} - \frac{10}{3}} \eta^{-\frac{10}{3}} \Gamma\left(\frac{10}{3} - \frac{r}{2}\right) L^4, & \gamma = 1 \\ \frac{1}{90} \alpha^{\frac{r}{4} - \frac{5}{3}} \eta^{-\frac{10}{3}} \Gamma\left(\frac{5}{3} - \frac{r}{4}\right) L^4, & \gamma = 2. \end{cases} \quad (18)$$

To assess the effect of finite outer scale, we evaluated the integrals leading to Equation (18) numerically, given that it was not possible to obtain closed forms. We found that these results agreed to numerical precision with Equation (18) for both values of γ . This suggests that the effect of an outer scale L_0 is negligible at short distances. This may not be surprising given that the beam is not exposed to large-scale effects when it propagates such short distances. We also note, as seen in Equation (18), that only the numerical value of the prefactors in $\overline{\chi^2}$ depends on γ and r while the power-law in L remains unaffected.

3.2.2. L^3 regime

For relatively larger distances that still satisfy $\sqrt{\lambda L} \ll \eta$, $\overline{\chi^2}$ is computed from Equation (15) with $F_{\chi\chi}^{(2)}(k)$ from Equation (7) and $F_{nn}(k)$ from Equation (17). Without making further simplifications, we obtain

$$\overline{\chi^2} = C_n^2 \frac{\pi \alpha^{\frac{3r-14}{6\gamma}} \Gamma\left(\frac{14-3r}{6\gamma}, \alpha \left(\frac{\eta}{L_0}\right)^\gamma\right)}{12\gamma \eta^{7/3}} L^3. \quad (19)$$

In the limit, $L_0 \rightarrow \infty$, the second term in the Gamma function vanishes and L_0 ceases to have an effect on $\overline{\chi^2}$. However, at finite (and especially low) Reynolds numbers, neglecting this term would lead to values of $\overline{\chi^2}$ much larger than the more complete expression Equation (19) including L_0 . We also note that similar to the L^4 regime, the power law in L^3 scaling is not affected by either γ or r and only the numerical value of the prefactors in $\overline{\chi^2}$ depends upon both of these parameters. For instance, for $\alpha = 8$ the value of $\overline{\chi^2}$ corresponding to $\gamma = 2$ is approximately 4.5 times larger than that for $\gamma = 1$. However, when $\alpha = 1$, as in Tatarski's work, then $\overline{\chi^2}$ with $\gamma = 2$ is only a small factor (~ 0.4) of its value corresponding to $\gamma = 1$.

3.2.3. $L^{11/6}$ regime

If one now considers even longer propagation distances within the range $\eta \ll \sqrt{\lambda L} \ll L_0$, the log-amplitude variance requires the evaluation of

$$\overline{\chi^2} = \frac{1}{2} \pi C_n^2 \int_{1/L_0}^{\infty} \kappa^2 L \left(1 - \frac{\kappa}{k^2 L} \sin \frac{k^2 L}{\kappa}\right) k^{-\frac{11}{3}} (k\eta)^{-\frac{r}{2}} \exp(-\alpha(\eta k)^\gamma) k dk, \quad (20)$$

which is obtained by substituting $F_{nn}(k)$ from Equation (17) in Equation (6). For the particular case of $\gamma = 2$, one can obtain a closed-form expression for $\overline{\chi'^2}$:

$$\overline{\chi'^2} = \frac{1}{8} \pi C_n^2 \kappa^2 L_0^{\frac{r}{2} + \frac{5}{3}} \eta^{-\frac{r}{2}} \left[2L E_{\frac{r}{4} + \frac{11}{6}} \left(\frac{\alpha \eta^2}{L_0^2} \right) + i \kappa L_0^2 \left\{ E_{\frac{r}{4} + \frac{17}{6}} \left(\frac{\alpha \eta^2 \kappa - iL}{\kappa L_0^2} \right) - E_{\frac{r}{4} + \frac{17}{6}} \left(\frac{\alpha \kappa \eta^2 + iL}{\kappa L_0^2} \right) \right\} \right], \quad (21)$$

where $E_n(z) = \int_0^\infty t^{-n} e^{-zt} dt$ is an exponential integral function. For the particular case of $L_0 \rightarrow \infty$ and $\gamma = 2$, Equation (20) yields a simpler form:

$$\overline{\chi'^2} = \frac{1}{48} \pi C_n^2 \eta^{5/3} \kappa^2 \alpha^{\frac{r}{4} + \frac{5}{6}} \Gamma \left(-\frac{r}{4} - \frac{11}{6} \right) \left\{ 12 \alpha \eta^2 \kappa \left(\frac{L^2}{\alpha^2 \eta^4 \kappa^2} + 1 \right)^{\frac{1}{24}(3r+22)} \sin \left(\frac{1}{12} (3r+22) \cot^{-1} \left(\frac{\alpha \eta^2 \kappa}{L} \right) \right) - L(3r+22) \right\} \quad (22)$$

While no power law in distance L is apparent in either Equation (21) or Equation (22), both of these expressions in fact include multiple scalings. For example, as we show later, $\overline{\chi'^2}$ from Equation (21) grows as L^3 initially followed by a transition to $L^{11/6}$ scaling and eventually, at very large distances, $\overline{\chi'^2}$ increases linearly with L . However, for Equation (22) which is obtained for an infinitely large outer-scale L_0 , the log-amplitude variance transitions from L^3 to $L^{11/6}$ and no further transition is observed.

There is ample evidence, however, as noted in the introduction, that $\overline{\chi'^2}$ is not unbounded, but instead tends to saturate at long distances. Thus Equation (22) is only expected to apply as intermediate asymptotics. It is also important to note here that Equation (20) does not yield the new L^4 regime for $\overline{\chi'^2}$, regardless of the limits of integral, since this expression only considers the effect of scales that satisfy condition given by Equation (4).

To assess the effect of varying γ , we evaluated the integral in Equation (20) numerically to compute $\overline{\chi'^2}$ at varying L . The results of this analysis are shown in Figure 1. We have verified the numerical integration by direct comparison with theoretical results in specific range and limits (e.g. Equation (21) with $\gamma = 2$ and finite L_0).

Three main conclusions can be drawn from Figure 1(a). First, γ clearly affects the magnitude of $\overline{\chi'^2}$ in the L^3 scaling region. Similar effect of γ on $\overline{\chi'^2}$ was also observed in the L^4 regime, which albeit not shown here, is evident from Equation (18). Second, $\overline{\chi'^2}$ approaches the same numerical value at large distance where it grows as L irrespective of γ . Lastly, in the intermediate region where the distance satisfies $\eta \ll \sqrt{\lambda L} \ll L_0$, there is a sharp transition from L^3 to $L^{11/6}$ scaling for $\gamma = 2$. However, this is not the case for lower γ values. For example, when $\gamma = 0.5$, there appears to be an additional transitional scaling region after L^3 and before $L^{11/6}$ is reached. While we could not obtain theoretical expressions for arbitrary γ , the numerical results suggest that the $L^{11/6}$ and L regimes of $\overline{\chi'^2}$ are independent of γ , as seen in Figure 1(a). Thus the theoretical expressions obtained for $\gamma = 2$ are adequate to quantify these two regimes of the variance of log-amplitude for all γ .

Because of the difficulty in assessing the effect of outer-scale in closed form directly from Equation (21) for general γ , we performed a numerical integration of this general expression. In Figure 1(b), we plot $\overline{\chi'^2}$ obtained from numerical evaluation of Equation (20)

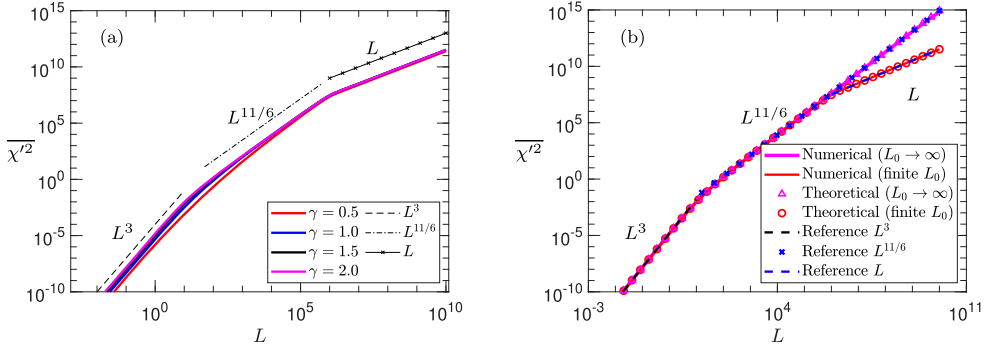


Figure 1. (a) Spatial variation of $\overline{\chi^2}$ for different γ and finite L_0 . (b) Comparison of theoretical and numerically integrated values of $\overline{\chi^2}$ for $\gamma = 2$. Different lines in (b) are: solid magenta: numerical with $L_0 \rightarrow \infty$, solid red: numerical with finite L_0 , triangles: theoretical (Equation 22) with $L_0 \rightarrow \infty$, circles: theoretical (Equation 21) with finite L_0 . Also shown in (b) are the theoretical limits in different scaling regimes: L^3 in dashed-black (Equation 19), $L^{11/6}$ in blue pluses (Equation 23) and L in dashed-blue (Equation 24). L^4 regime is not included here.

for finite L_0 for varying L in solid red line for $\gamma = 2$. The theoretical expression given by Equation (21) is also shown in red circles to validate the numerical integration. As expected, the results from both approaches are in excellent agreement and there is a transition from $L^{11/6}$ to L as the distance increases. If instead, the integral in Equation (20) is computed such that $L_0 \rightarrow \infty$, then the numerical integration gives the magenta line in Figure 1(b) which agrees exactly with the corresponding theoretical expression given by Equation (22) (triangles). In this case, $\overline{\chi^2}$ continues to grow as $L^{11/6}$ indefinitely. Thus the linear scaling of variance of log-amplitude fluctuations with distance only appears if the integral in Equation (21) is evaluated for finite L_0 . Alternatively, when the outer scale tends to infinity, the transition to linear scaling will occur at infinite propagation distance. Since both Equations (21) and (22) exhibit different behaviors at large L , we can obtain two distinct scaling laws by taking appropriate limits for each of these.

To obtain the asymptotic behavior of $\overline{\chi^2}$ at large distance but that still satisfy $\eta \ll \sqrt{\lambda L} \ll L_0$, we follow the approach in [30] which introduces a new variable $\delta = \eta \sqrt{\alpha \kappa / L}$ in Equation (22) and then evaluates the limit $\delta \rightarrow 0$ to yield,

$$\overline{\chi^2} = \frac{1}{4} C_n^2 \pi \kappa^{\frac{7}{6} - \frac{r}{4}} \eta^{-\frac{r}{2}} \sin\left(\frac{1}{24} \pi (3r + 22)\right) \Gamma\left(-\frac{r}{4} - \frac{11}{6}\right) L^{\frac{r}{4} + \frac{11}{6}} \quad (23)$$

for $\gamma = 2$. The blue cross in Figure 1(b) represents Equation (23) for $r = 0$. It is interesting to note here that unlike in L^3 and L^4 regimes, intermittency does change the exponent of L in the $11/6$ regime. More precisely, it steepens the slope of $\overline{\chi^2}$ by a factor of $r/4$. While the parameter r is small, not accounting for its effects on the measurements especially at large distances could yield inaccurate calculations of for example C_n^2 or correction metrics in adaptive optics. For illustration, if one considers a Kolmogorov length-scale $\eta = 1$ mm, and an optical wavelength $\lambda = 1 \mu$ m, then the structure-function parameter C_n^2 computed from Equation (23) for $\overline{\chi^2}$ measured at $L = 800$ m is about 20% larger if $r = 0$ is used instead of $r = 0.2$. Alternatively, for a known C_n^2 , the variance of log-amplitude fluctuations given by Equation (23) is larger for $r > 0$ than that for $r = 0$. Thus $\overline{\chi^2}$ will approach the so-called

saturation at values close to unity at a relatively shorter distance for a non-zero r . For example, if $C_n^2 = 10^{-13} \text{m}^{-2/3}$, $\eta = 1 \text{ mm}$ and $\lambda = \mu\text{m}$, then $\overline{\chi^2}$ estimated from Equation (23) will reach unity at about 50 m earlier when intermittency corrections are included ($r = 0.2$).

3.2.4. L^1 regime

Lastly, when the propagation distance is very large ($\sqrt{\lambda L} \gg L_0$), we take the limit $L \rightarrow \infty$ in Equation (21), to obtain the linear scaling law,

$$\overline{\chi^2} = \frac{1}{4} \pi C_n^2 \eta^{5/3} \kappa^2 \alpha^{r/4 + 5/6} \Gamma\left(-\frac{r}{4} - \frac{5}{6}, \frac{\alpha \eta^2}{L_0^2}\right) L, \quad (24)$$

where $\Gamma(a, z) = \int_z^\infty t^{a-1} e^{-t} dt$ is the incomplete gamma function. This expression is also plotted in Figure 1(b) for $r = 0$ as a dotted blue line. In Equation (24) r only affects the prefactors of $\overline{\chi^2}$ but not the scaling with L . At large distances, numerical integration suggests that both Equations (23) and (24) are valid for all γ even though the expressions were obtained for $\gamma = 2$.

3.3. Phase variation

Following the procedure in previous sections, we can also derive scaling laws for the variance of phase distortions. Here again, we find a previously unknown regime at short distances when the effect of large scales not accounted for in classical work [2] is incorporated in the analysis. Mathematically, this implies relaxing Equation (4).

3.3.1. L^2 regime

We start by directly considering the general form of the spectral density of fluctuations in phase that can be found in, e.g. [2, 30]:

$$F_{SS}^{(2)}(k) \approx \kappa^2 L \int_0^L \left\{ 1 + \frac{\kappa}{k^2 L} \sin \frac{k^2 L}{\kappa} - \frac{\xi}{2L} \left(3 + \cos \frac{k^2 L}{\kappa} \right) \right\} \left(\int_{-\infty}^{\infty} \cos(k_1 \xi) F_{nn} \left(\sqrt{k_1^2 + k^2} \right) dk_1 \right) d\xi. \quad (25)$$

A more general expression for spectrum of fluctuations in phase is also discussed in [55]. Similar to the log-amplitude fluctuations, the variance of the fluctuations in phase can then be computed using

$$\overline{S^2} = 2\pi \int_{1/L_0}^{\infty} F_{SS}^{(2)}(k) k dk. \quad (26)$$

At very short distances, in the limit $L \rightarrow 0$, we can combine Equations (25) and (26) to obtain

$$\overline{S^2} = -\frac{C_n^2 \pi \kappa^2}{4L_0 \Gamma\left(\frac{r}{4} + \frac{11}{6}\right)} \left(\sqrt{\pi} \eta^{8/3} \alpha^{r/4 + 4/3} \csc\left(\frac{1}{12} \pi (3r + 4)\right) \Gamma\left(\frac{r}{4} + \frac{11}{6}\right) \right. \\ \left. {}_2F_2\left(\frac{1}{2}, \frac{1}{2}; \frac{r}{4} + \frac{7}{3}, \frac{3}{2}; -\frac{\alpha \eta^2}{L_0^2}\right) \right)$$

$$\begin{aligned}
 & - \frac{12L_0^{\frac{r}{2}+\frac{8}{3}}\eta^{-\frac{r}{2}}\Gamma\left(\frac{r}{4}+\frac{4}{3}\right) {}_2F_2\left(-\frac{r}{4}-\frac{5}{6},-\frac{r}{4}-\frac{5}{6};-\frac{r}{4}-\frac{1}{3},\frac{1}{6}-\frac{r}{4};-\frac{\alpha\eta^2}{L_0^2}\right)}{\sqrt{\pi}(3r+10)} \\
 & + \pi\eta^{5/3}L_0\alpha^{\frac{r}{4}+\frac{5}{6}}\sec\left(\frac{1}{12}\pi(3r+4)\right) L^2, \tag{27}
 \end{aligned}$$

where F_{nn} from Equation (17) is substituted with $\gamma = 2$. We can see that the variance of phase fluctuations increases with distance L in proportion to L^2 . This is also a new scaling regime at short distances that has not been reported in previous works. On taking a Taylor series expansion of Equation (27) at L_0 equal to infinity, a simplified scaling law is obtained,

$$\overline{S^2} = \frac{C_n^2\kappa^2\sqrt{\pi}L_0^{2/3}\Gamma\left(\frac{1}{3}\right)}{4\Gamma\left(\frac{11}{6}\right)}L^2. \tag{28}$$

This expression is also recovered in the limit $\eta \rightarrow 0$. Thus both these distinct ways of approaching an infinite Reynolds number yield Equation (28).

3.3.2. L^1 regime

At comparatively larger distances, the variance of the fluctuations in phase can be accurately computed by considering only wavenumbers that satisfy $1/k \ll L$, as done in classical work [2]. Equation (25) can then be expressed in a simplified form

$$F_{SS}^{(2)}(k) = \pi\kappa^2L\left(1 + \frac{\kappa}{k^2L}\sin\frac{k^2L}{\kappa}\right)F_{nn}(k), \tag{29}$$

where Equation (5) is also utilized. For propagation distances that satisfy $\sqrt{\lambda L} \ll \eta$, Equation (29) can be further simplified to

$$F_{SS}^{(2)}(k) = 2\pi\kappa^2LF_{nn}(k). \tag{30}$$

This allows the computation of the variance of fluctuations in phase using Equation (26). The result is

$$\overline{S^2} = \frac{1}{\gamma}C_n^2\pi\kappa^2LL_0^{\frac{r}{2}+\frac{5}{3}}\eta^{-\frac{r}{2}}\left(\alpha\left(\frac{\eta}{L_0}\right)^\gamma\right)^{\frac{3r+10}{6\gamma}}\Gamma\left(-\frac{3r+10}{6\gamma},\alpha\left(\frac{\eta}{L_0}\right)^\gamma\right). \tag{31}$$

Thus $\overline{S^2}$ transitions from L^2 to L as the distance increases. A more general expression for $\overline{S^2}$ can be directly computed if Equation (29) is used in Equation (26) to yield:

$$\begin{aligned}
 \overline{S^2} = C_n^2\pi\kappa^2 & \left\{ \frac{1}{4}L_0^{\frac{r}{2}+\frac{5}{3}}\eta^{-\frac{r}{2}}E_{\frac{r}{4}+\frac{11}{6}}\left(\frac{\alpha\eta^2}{L_0^2}\right)L \right. \\
 & \left. - \frac{1}{8}i\kappa L_0^{\frac{r}{2}+\frac{11}{3}}\eta^{-\frac{r}{2}}E_{\frac{r}{4}+\frac{17}{6}}\left(\frac{\alpha\eta^2\kappa-iL}{\kappa L_0^2}\right) + \frac{1}{8}i\kappa L_0^{\frac{r}{2}+\frac{11}{3}}\eta^{-\frac{r}{2}}E_{\frac{r}{4}+\frac{17}{6}}\left(\frac{\alpha\kappa\eta^2+iL}{\kappa L_0^2}\right) \right\} \tag{32}
 \end{aligned}$$

for $\gamma = 2$. It is interesting to note here that the closed-form expressions for the variance of phase fluctuations could only be obtained by considering finite-outer scale L_0 . In other words, if the lower limit of integration in Equation (26) is zero, then the integral does not

converge. The variance of fluctuations in phase given by Equation (32) exhibits two limiting behaviors,

$$\overline{S^2} = C_n^2 \pi \eta^{5/3} \kappa^2 \alpha^{\frac{r}{4} + \frac{5}{6}} \Gamma \left(-\frac{r}{4} - \frac{5}{6}, \frac{\alpha \eta^2}{L_0^2} \right) L \begin{cases} \frac{1}{2}, & 0 \ll \sqrt{\lambda L} \ll \eta \\ \frac{1}{4}, & \eta \ll \sqrt{\lambda L}, \end{cases} \quad (33)$$

both of which grow linearly with L , with the latter limit being half of the former in magnitude. The first expression in Equation (33) is equal to Equation (31) when $\gamma = 2$. A simplified expression for the phase variance using the so-called von Karman spectrum for the refractive index was derived in [56] which also showed a linear scaling with L , i.e. $\overline{S^2} \sim L$. It is also interesting to note here that at very large L , the variance of both phase and log-amplitude fluctuations is proportional to L and take the exact same functional form. This has been noted before for structure functions of amplitude and phase fluctuations [30]. While the integral in Equation (26) does not converge for $L_0 \rightarrow \infty$, the limiting behavior can still be obtained by taking a Taylor series expansion of Equation (33) about $L_0 = \infty$ to yield

$$\overline{S^2} = C_n^2 \pi \kappa^2 \left(\frac{12\eta^{-\frac{r}{2}}}{3r + 10} \right) L_0^{\frac{r}{2} + \frac{5}{3}} L \begin{cases} \frac{1}{2}, & 0 \ll \sqrt{\lambda L} \ll \eta \\ \frac{1}{4}, & \eta \ll \sqrt{\lambda L}. \end{cases} \quad (34)$$

4. Transition between different scaling regimes

The scaling laws for variance in phase or log-amplitude listed in the previous section are derived as an asymptotic behavior with respect to the propagation length (L or $\sqrt{\lambda L}$) in comparison to characteristic length scales of turbulence. It is, therefore, also important to obtain the propagation distance L at which the transition between different regimes occurs. This is useful information when interpreting and even designing experiments. It is also critical if one attempts to determine C_n^2 , for example, using specific scaling laws such as Equation (22) in the $L^{11/6}$ regime.

We first look at the transitions in the scaling of log-amplitude variance. The transition from L^4 to L^3 can be computed simply by equating Equations (18) and (19). The result, denoted by $L_{4 \rightarrow 3}$, is given by

$$L_{4 \rightarrow 3} = \begin{cases} \frac{15\pi\alpha\eta\Gamma\left(\frac{7}{3} - \frac{r}{2}, \frac{\alpha\eta}{L_0}\right)}{4\Gamma\left(\frac{10}{3} - \frac{r}{2}\right)}, & \gamma = 1 \\ \frac{15\pi\sqrt{\alpha}\eta\Gamma\left(\frac{7}{6} - \frac{r}{4}, \frac{\alpha\eta^2}{L_0^2}\right)}{4\Gamma\left(\frac{5}{3} - \frac{r}{4}\right)}, & \gamma = 2. \end{cases} \quad (35)$$

Clearly this transition distance depends closely on the small-scale characteristics of turbulence (η , γ and α), as expected. The next transition is from L^3 to $L^{\frac{11}{6} + \frac{r}{4}}$ (or $L^{\frac{11}{6}}$ without intermittency corrections) and is computed by solving Equations (19) and (23) simultaneously.

The result is

$$L_{3 \rightarrow \frac{11}{6}} = \eta^2 \kappa 3^{\frac{12}{14-3r}} \alpha^{\frac{2}{\gamma}} \gamma^{\frac{12}{14-3r}} \sin^{\frac{12}{14-3r}} \left(\frac{1}{24} \pi (3r + 22) \right) \Gamma \left(-\frac{r}{4} - \frac{11}{6} \right)^{\frac{12}{14-3r}} \Gamma \left(\frac{14-3r}{6\gamma}, \alpha \left(\frac{\eta}{L_0} \right)^\gamma \right)^{\frac{12}{3r-14}}. \quad (36)$$

For $\gamma = 2$, Equation (36) gives an accurate measurement of transition between two adjacent regimes. However, for $\gamma < 2$, as described in the previous section, there exists an intermediate region with a much smoother transition between L^3 and $L^{11/6}$. Thus, in such cases, Equation (36) is not a pointwise prediction of where the power law transitions between the two regimes. Instead, Equation (36) only gives a distance around which this smooth transition happens.

Finally, the transition between $L^{\frac{11}{6}}$ and L is given by

$$L_{\frac{11}{6} \rightarrow 1} = \alpha \eta^2 \kappa \sin^{-\frac{12}{3r+10}} \left(\frac{1}{24} \pi (3r + 22) \right) \Gamma \left(-\frac{r}{4} - \frac{11}{6} \right)^{-\frac{12}{3r+10}} \Gamma \left(-\frac{r}{4} - \frac{5}{6}, \frac{\alpha \eta^2}{L_0^2} \right)^{\frac{12}{3r+10}}, \quad (37)$$

and is observed only if the outer-scale L_0 is finite. For simplicity, we list these transition distances in Table 1 for $r = 0$ and $\gamma = \{1, 2\}$. Under certain conditions, one or more of the intermediate scaling regimes can be non-existent. For example, there can be a direct transition from L^4 to $L^{\frac{11}{6}}$ or even to L . Similarly, and as pointed out in [2], in the absence of scale separation, $\overline{\chi^2}$ directly grows linearly with L after L^3 regime. For completion these transition distances are also included in Table 1.

Also listed in Table 1 is the different transition distances obtained in the limit when the smallest scale of turbulence (η) goes to zero and the large-scale (L_0) tends to infinity. These two cases represent two distinct ways of approaching the infinite Reynolds number limit. Note that the former limit is physically meaningful only if the optical wavelength itself also approaches zero to ensure that the paraxial approximation is satisfied. Thus its unqualified application to physically relevant conditions may be narrow. Still as we see from the table, the variance in log-amplitude fluctuations exhibits only $L^{11/6}$ and L regimes since the transition from L^4 to L^3 and L^3 to $L^{11/6}$ occurs at $L = 0$.

In the other limit, that is $L_0 \rightarrow \infty$, we see that there is no transition to the linear L regime as noted in the previous section. A unique characteristic of the $L^4 - L^3$ transition is that the transition distance is independent of the optical wavenumber. The strong dependence of the transition distance on small scale characteristics of turbulence (α , η and γ) highlights the importance of accurate determination of these quantities.

We close this section by listing the only transition predicted by the theory for the variance of phase fluctuations, namely from L^2 to linear scaling in L :

$$L_{2 \rightarrow 1} = \frac{\alpha^{-\frac{r}{4} - \frac{5}{6}} \left(2\Gamma \left(-\frac{1}{3} \right) \Gamma \left(\frac{11}{6} \right) \sqrt[3]{\alpha \eta^2} {}_1F_1 \left(-\frac{1}{2}; \frac{4}{3}; -\frac{\alpha \eta^2}{L_0^2} \right) + \sqrt{\pi} L_0^{2/3} \Gamma \left(\frac{1}{3} \right) {}_1F_1 \left(-\frac{5}{6}; \frac{2}{3}; -\frac{\alpha \eta^2}{L_0^2} \right) \right)}{2\pi \eta^{5/3} \Gamma \left(\frac{11}{6} \right) \Gamma \left(-\frac{r}{4} - \frac{5}{6}, \frac{\alpha \eta^2}{L_0^2} \right)}. \quad (38)$$

This transition, obtained by dividing the first equation in Equation (33) with Equation (27), is independent of the optical wavelength.

Table 1. Transition distances for when $r = 0$.

Transition	$\gamma = 1$	$\gamma = 2$
$L_{4 \rightarrow 3}$	$\frac{15\pi\alpha\eta\Gamma(\frac{7}{3}, \frac{\alpha\eta}{L_0^2})}{4\Gamma(\frac{10}{3})} = \begin{cases} 0, & \eta \rightarrow 0 \\ 5.05\alpha\eta, & L_0 \rightarrow \infty \end{cases}$	$\frac{15\pi\sqrt{\alpha}\eta\Gamma(\frac{7}{6}, \frac{\alpha\eta^2}{L_0^2})}{4\Gamma(\frac{5}{3})} = \begin{cases} 0, & \eta \rightarrow 0 \\ 12.11\sqrt{\alpha}\eta, & L_0 \rightarrow \infty \end{cases}$
$L_{3 \rightarrow \frac{11}{6}}$	$\frac{\alpha^2\eta^2\kappa(3(\sqrt{3}-1)\Gamma(-\frac{11}{6}))^{6/7}}{2^{22/7}\Gamma(\frac{7}{3}, \frac{\alpha\eta}{L_0^2})^{6/7}} = \begin{cases} 0, & \eta \rightarrow 0 \\ 2.10\alpha^2\eta^2\kappa, & L_0 \rightarrow \infty \end{cases}$	$\frac{\alpha\eta^2\kappa(3(\sqrt{3}-1)\Gamma(-\frac{11}{6}))^{6/7}}{2^{3/7}\Gamma(\frac{7}{6}, \frac{\alpha\eta^2}{L_0^2})^{6/7}} = \begin{cases} 0, & \eta \rightarrow 0 \\ 4.71\alpha\eta^2\kappa, & L_0 \rightarrow \infty \end{cases}$
$L_{\frac{11}{6} \rightarrow 1}$	$\frac{2^{24/5}\alpha\eta^2\kappa\Gamma(-\frac{5}{6}, \frac{\alpha\eta^2}{L_0^2})^{6/5}}{((\sqrt{3}-1)\Gamma(-\frac{11}{6}))^{6/5}} = \begin{cases} 1.34\kappa L_0^2, & \eta \rightarrow 0 \\ \infty, & L_0 \rightarrow \infty \end{cases}$	
$L_{4 \rightarrow \frac{11}{6}}$	$\frac{3^{12}\kappa^{\frac{7}{13}}(\frac{5(\sqrt{3}-1)\pi\Gamma(-\frac{11}{6})}{\Gamma(\frac{10}{3})})^{\frac{6}{13}}(\alpha\eta)^{\frac{20}{13}}}{2 \cdot 2^{\frac{8}{13}}} = \begin{cases} 0, & \eta \rightarrow 0 \\ 3.15\kappa^{\frac{7}{13}}(\alpha\eta)^{\frac{20}{13}}, & L_0 \rightarrow \infty \end{cases}$	$\frac{3^{12}\kappa^{\frac{7}{13}}(\frac{5(\sqrt{3}-1)\pi\Gamma(-\frac{11}{6})}{\Gamma(\frac{5}{3})})^{\frac{6}{13}}(\alpha\eta^2)^{\frac{10}{13}}}{2 \cdot 2^{\frac{2}{13}}} = \begin{cases} 0, & \eta \rightarrow 0 \\ 7.28\kappa^{\frac{7}{13}}(\alpha\eta^2)^{\frac{20}{13}}, & L_0 \rightarrow \infty \end{cases}$
$L_{4 \rightarrow 1}$	$(\frac{3}{2})^{2/3}\alpha^{25/18}\sqrt[3]{\frac{5\pi}{\Gamma(\frac{10}{3})}}\sqrt[3]{\eta^5\kappa^2\Gamma(-\frac{5}{6}, \frac{\alpha\eta^2}{L_0^2})} = \begin{cases} 0, & \eta \rightarrow 0 \\ \infty, & L_0 \rightarrow \infty \end{cases}$	$3^{2/3}\alpha^{5/6}\sqrt[3]{\frac{5\pi}{2\Gamma(\frac{5}{3})}}\sqrt[3]{\eta^5\kappa^2\Gamma(-\frac{5}{6}, \frac{\alpha\eta^2}{L_0^2})} = \begin{cases} 0, & \eta \rightarrow 0 \\ \infty, & L_0 \rightarrow \infty \end{cases}$
$L_{3 \rightarrow 1}$	$\alpha^{19/12}\eta^2\kappa\sqrt{\frac{3}{\Gamma(\frac{7}{3})}}\sqrt{\Gamma(-\frac{5}{6}, \frac{\alpha\eta^2}{L_0^2})} = \begin{cases} 0, & \eta \rightarrow 0 \\ \infty, & L_0 \rightarrow \infty \end{cases}$	$\alpha\eta^2\kappa\sqrt{\frac{6}{\Gamma(\frac{6}{6})}}\sqrt{\Gamma(-\frac{5}{6}, \frac{\alpha\eta^2}{L_0^2})} = \begin{cases} 0, & \eta \rightarrow 0 \\ \infty, & L_0 \rightarrow \infty \end{cases}$

5. Non-dimensionalization of scaling laws and transitions

The scaling laws and the transition distances obtained in the previous sections depend upon several length scales and dimensional parameters characterizing both optical wavelength and the relevant turbulent scales. In this section, we identify relevant set of non-dimensional parameters that can be used to completely quantify evolution of the variance of log-amplitude in all scaling regimes. These parameters can also be used to obtain universal forms of other relevant quantities such as the spectral density of phase and log-amplitude fluctuations. The value of such universal forms is that they facilitate comparisons between simulations and experiments at different conditions. An important dimensional parameter that appears in all the regimes for both phase and log-amplitude variance is the so-called structure function parameter C_n^2 . This is discussed first.

5.1. Structure function parameter C_n^2

The second-order structure function of the fluctuations in refractive index is defined as

$$D_n(d) \equiv \langle [n(x+d) - n(x)]^2 \rangle, \quad (39)$$

where d is the separation distance [2, 11]. For isotropic, homogeneous turbulence at a sufficiently large Reynolds number, when the separation distance is within the inertial range of scales (i.e. $\eta \ll d \ll L_0$) a ‘two-thirds’ scaling law is obtained

$$D_n(d) = C_n^2 d^{2/3}, \quad (40)$$

based on Kolmogorov similarity hypotheses [11]. Here C_n^2 is the refractive index structure function parameter with units $m^{-2/3}$ and has been extensively used as a metric to quantify the strength of turbulence in aero-optical studies. One of the most common ways in which C_n^2 is obtained in experiments is by equating the measured value of the variance in log-amplitude fluctuations at some propagation distance with a theoretical expression, such as Equation (10) [19, 57, 58]. Alternatively, C_n^2 can be expressed in terms of the structure function parameter for temperature fluctuations (C_T^2) which in turn is computed from the measured value of the corresponding structure function [17, 59]. While several models [1] based on experimental measurements have been proposed to characterize the average C_n^2 , there is a wide disparity in its measured value since it depends upon local flow conditions, time of measurement, altitude, terrain, humidity, etc. It is thus not surprising that C_n^2 has been observed to span several orders of magnitude (10^{-18} to $10^{-8} m^{-2/3}$) with the higher end of this range relevant in aero-optics and the lower values more prominent in atmospheric turbulence [1, 21, 58]. This adds complexity to any attempt to compare data across different experimental studies.

At sufficiently high Reynolds number, Kolmogorov theory predicts a well-defined inertial range where Equation (40) holds. In such a case, one would see a clear plateau if one plots of compensated structure function $D_n(d)/d^{2/3}$. The parameter C_n^2 then simply corresponds to the height of the plateau so obtained. This approach has been used in incompressible turbulence to determine the structure function constant for velocity and passive scalars, anomalous scaling exponents, and other quantities of interest [60–64]. However, in the absence of inertial range there is no clear plateau in the compensated structure function.

In that case, one may still obtain an estimate for the value of C_n^2 according to

$$C_n^2 = \max\left(\frac{D_n(d)}{d^{2/3}}\right). \quad (41)$$

Similar estimations have been utilized in computation of Lagrangian structure function constant [65] and velocity structure function constant in isotropic turbulence [62]. Of course, as one increases the Reynolds number, an estimation like Equation (41) is expected to asymptote to the correct high- R_Λ value as a well-defined scaling range develops. In the case of compressible (or variable-density) turbulence, other parameters are needed to characterize the state of the flow. In general, fluctuations of both hydrodynamic and thermodynamic variables depend on the Reynolds number, turbulent Mach number and the relative strength of dilatational modes compared to the solenoidal modes. Here we will use the so-called Taylor Reynolds number

$$R_\Lambda \equiv \langle \rho \rangle u_{\text{rms}} \lambda / \mu,$$

where the Taylor scale is defined as $\Lambda = u_{\text{rms}} / \langle (\partial u / \partial x)^2 \rangle^{1/2}$ and μ is the mean viscosity. The turbulent Mach number is

$$M_t \equiv u_{\text{rms}} / c,$$

where c is the mean speed of sound. Finally, using Helmholtz decomposition we can separate the solenoidal (incompressible) velocity, \mathbf{u}_s , and potential (compressible) field, \mathbf{u}_d , such that $\mathbf{u} = \mathbf{u}_s + \mathbf{u}_d$ with $\nabla \cdot \mathbf{u}_s = 0$ and $\nabla \times \mathbf{u}_d = 0$. The relative contribution of these modes is given by

$$\delta = u_{d,\text{rms}} / u_{s,\text{rms}},$$

where $u_{s,\text{rms}}$ and $u_{d,\text{rms}}$ are the rms of the solenoidal and dilatational components, respectively. These three parameters have been shown to provide a complete characterization of the statistical state of compressible turbulence [66].

To test the theoretical results presented here, starting from the structure function parameter C_n^2 in Equation (40), we use a large database of well-resolved direct numerical simulations (DNS) where all temporal and spatial scales of the turbulence are appropriately resolved. In particular, the fully compressible Navier–Stokes equations along with a perfect gas state equation are solved using tenth-order compact difference schemes and explicit third-order Runge–Kutta schemes in space and time, respectively. These simulations are conducted in a triply-periodic domain and the large scales are forced. Our database covers a range of Reynolds numbers (R_Λ), turbulent Mach numbers (M_t), and forcing parameter (σ). The parameter σ acts a weighting factor in the forcing term and controls the amount of forcing introduced into the solenoidal component of the velocity field (\mathbf{u}_s) relative to its dilatational counterpart (\mathbf{u}_d). When $\sigma = 100\%$, only the solenoidal field is forced and when $\sigma = 0\%$, only the dilatational field is forced. The rationale for this forcing approach is that σ is intimately linked to the magnitude of the fluctuations in the density field (see, e.g. [66–68]). By decreasing σ , that is by increasing the forcing in the dilatational modes, the magnitude of density fluctuations also increases [66]. The Prandtl number for each of these simulations is 0.72, which is the case for air, and thus relevant to propagation through the atmosphere. In Table 2, we summarize some important parameters of the simulations

Table 2. Direct numerical simulation (DNS) parameters: grid resolution (N^3), Reynolds and turbulent Mach numbers (R_Λ, M_t), ratio of solenoidal to dilatational forcing (σ), ratio of $\delta = u_{d,rms}/u_{s,rms}$ structure parameter $C_n^2 \times L_0^{2/3}$, ratio on integral and Kolmogorov length scales of density fluctuations (L_ρ/η).

N	R_Λ	M_t	σ	δ	$C_n^2 \times L_0^{2/3}$	L_ρ/η
64	20	0.3	80%	1.24e-01	1.22e-10	1.01e+01
64	20	0.3	50%	5.19e-01	1.53e-09	7.71e+00
64	38	0.4	100%	1.04e-01	3.81e-10	1.91e+01
256	60	0.2	30%	1.49e-00	7.31e-10	3.76e+01
256	100	0.3	100%	1.02e-01	2.10e-10	6.46e+01
256	100	0.6	100%	1.95e-01	1.88e-09	4.33e+01
512	160	0.2	60%	3.37e-01	5.35e-10	8.01e+01
1024	240	0.5	70%	2.19e-01	9.27e-10	7.93e+01

including grid resolution, Reynolds number, turbulent Mach number, forcing parameter, and the ratio of length scales of turbulent field.

The normalized refractive index structure function for all the cases listed in Table 2 is shown in Figure 2(a). No clear plateau is observed in any of these cases. The C_n^2 computed using Equation (41) is shown in Figure 3(a) against the *rms* value of density fluctuations. As expected C_n^2 increases (by almost two orders of magnitude) with the intensity of density fluctuations. We also note that no systematic trend is obtained if C_n^2 is plotted against one of the governing parameters of the turbulence, that is, R_Λ or M_t . A complimentary view is given in Figure 2(a) where we show the spectrum of refractive index fluctuations $E_n(k) = 4\pi k^2 \Phi_n(k)$. Also added is a black-dashed reference line depicting the classical Kolmogorov 5/3 scaling law in the inertial range. While an incipient inertial range can be seen for the case $(R_\Lambda, M_t, \sigma) = (100, 0.3, 100\%)$, none of the other cases exhibit a 5/3 scaling and are clearly not in line with [11]. At higher levels of dilatational forcing, we see that the spectrum exhibits a single power-law scaling throughout all scales, for example case (60, 0.2, 30%). These illustrate clear departures from Kolmogorov scaling in compressible turbulence, not accounted for in classical theories [2]. However, by adjusting the parameters (r, γ, α) in the model spectrum in Equation (17) that we use for the theoretical analysis, a reasonable fit for

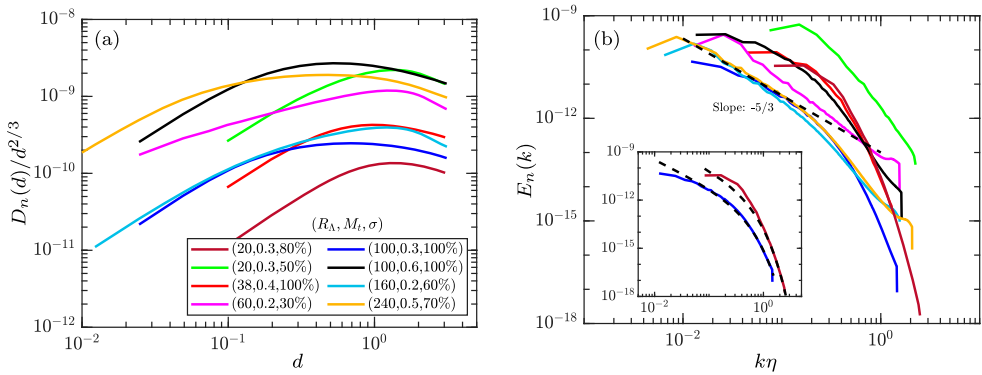


Figure 2. (a) Compensated second-order structure function and (b) spectrum of refractive index fluctuations. Different solid lines represent the cases listed in Table 2. Inset in (b) shows case (20, 0.3, 80%) and case (100, 0.3, 100%) with dashed-black line depicting model spectrum from Equation (17) with appropriate parameters.

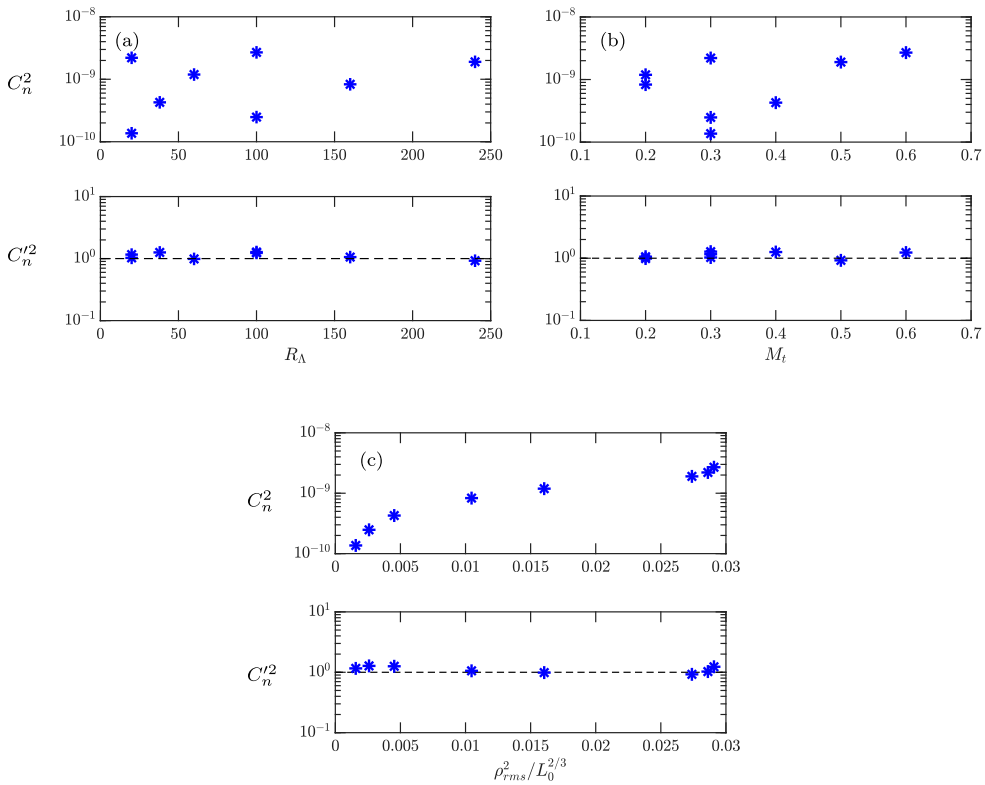


Figure 3. Variation of C_n^2 (top row) and $C_n'^2$ (bottom row) with (a) R_Λ , (b) M_t and (c) $\rho_{rms}^2 L_0^{2/3}$. The dashed line in bottom row plots denotes a $C_n'^2$ value of unity.

refractive index spectra can be obtained. This is shown in the inset of Figure 2(b) with $\gamma = 1$ and $\alpha \approx 5$ for two DNS cases. The departures at large scales at which forcing is applied are expected given the non-universal nature of these motions.

In either physical or spectral space, the structure function parameter C_n^2 characterizes the strength of the fluctuations in refractive index and appears as a multiplicative constant in the formulae for variances for log-amplitude and phase. However, because of its definition (Equation 40) C_n^2 is a dimensional quantity which will depend among other things on the size of the system. It is thus obvious that C_n^2 is not expected to be a universal constant of the governing parameters of the flow (e.g. R_Λ and M_t). This is clearly seen in Figure 3(a,b).

From a modeling perspective, it is thus more convenient to identify non-dimensional factors which, while weakly dependent on details of the large scale features of the flow, allows us to isolate self-similar aspects of the phenomenon by proper non-dimensionalization using suitable characteristics scales. A prime example is Kolmogorov constant for the energy spectrum which is an $O(1)$ constant for a wide range of flows and Reynolds numbers [54, 61, 69, 70].

A similar approach can be attempted for C_n^2 . For this, we note that as $d \gtrsim L_0$, where L_0 is the integral length scale for the refractive index (or density), the fluctuations separated by

this distance become uncorrelated and, trivially, one finds that $D_n(d)$ is twice the variance of the refractive index, that is, $D_n(L_0) \approx 2\overline{n^2}$. A natural way to normalize Equation (40) is by using $\overline{n^2}$ and L_0 :

$$\frac{D_n(d)}{\overline{n^2}} = C_n'^2 \left(\frac{d}{L_0} \right)^{2/3}, \quad (42)$$

where

$$C_n'^2 = \frac{C_n^2 L_0^{2/3}}{\langle n^2 \rangle}. \quad (43)$$

Note that if we evaluate Equation (42) at $d \rightarrow L_0$, we find that $C_n'^2$ must be order unity. This is in fact what we observe from DNS data in Figure 3(c) where $C_n'^2$ is indeed close to 1 (dashed line) for all conditions in our database. Since this involves a wide range of conditions including Reynolds and Mach numbers as well as combination of solenoidal and dilatational forcing, this approach suggest that $C_n'^2$ is an appropriate universal constant, though one cannot rule out weak dependencies in its numerical value on geometrical details of the flow. This approach also exposes the independent contributions of strength of fluctuations (through $\overline{n^2}$) and scale of the system (through L_0). The difficulties associated with the traditional C_n^2 combining both effects have been already identified in [71]. The explicit contribution from strength and length scales is also useful in trying to reproduce, e.g. atmospheric conditions in a small scale laboratory facility. For example, if the apparatus in the laboratory is 10 times smaller than the actual system, then $\overline{n^2}$ must be about 4.6 smaller than that in the actual system to retain the same $C_n'^2$. On the other hand, as discussed in Section 4 and in the next section, transitions between regimes depend on ratio of length scales involving L_0 which can also be important in scaling realistic flows to laboratory setups.

5.2. Universal scaling regimes and transition distances

With the new definition of $C_n'^2$, it is possible to rewrite the scaling regimes and all the transitions for the variance of log-amplitude fluctuations in a universal form. As we will see momentarily, this also facilitates the identification of the relevant normalized length scales in each regime. For brevity, here we only consider a specific case where $\gamma = 2$ and $r = 0$. The approach can be similarly extended to other values of γ and r . Note that to generalize this non-dimensionalization to arbitrary values of r , Equation (40) or Equation (43) will also need to be re-defined to include the effect of parameter r on scaling exponent. This would also include departures from the classical two-thirds scaling law due to high levels of compressibility.

On substitution of $C_n'^2$ using Equation (43) with the refractive index variance written in terms of density fluctuations via the Gladstone–Dale constant ($\overline{n^2} = K_{GD}^2 \rho_{rms}^2$) and using the well-known Kolmogorov relation $L_0/\eta = R_{L_0}^{3/4}$, we can readily write χ'^2 in the different scaling regimes as

$$\overline{\chi'^2} = C_n^2 \rho_{\text{rms}}^2 K_{GD}^2 \begin{cases} C_4 \alpha^{-5/3} R_{L_0}^{5/2} \left(\frac{L}{L_0}\right)^4, & L \ll \eta \\ C_3 \alpha^{-7/6} R_{L_0}^{7/4} \Gamma\left(\frac{7}{6}, \alpha R_{L_0}^{-3/2}\right) \left(\frac{L}{L_0}\right)^3, & \sqrt{\lambda L} \ll \eta \\ C_{11/6} \left(\frac{L_0}{\lambda}\right)^{7/6} \left(\frac{L}{L_0}\right)^{11/6} = C_{11/6} R_{L_0}^{7/8} \left(\frac{\eta}{\lambda}\right)^{7/6} \left(\frac{L}{L_0}\right)^{11/6}, & \eta \ll \sqrt{\lambda L} \ll L_0 \\ C_1 \alpha^{5/6} R_{L_0}^{-5/4} \Gamma\left(-\frac{5}{6}, \alpha R_{L_0}^{-3/2}\right) \left(\frac{L_0}{\lambda}\right)^2 \left(\frac{L}{L_0}\right), & L_0 \ll \sqrt{\lambda L} \end{cases} \quad (44)$$

The constants above are $C_4 = 4\Gamma(-4/3)/1215 \approx 0.0101$, $C_3 = \pi/6 \approx 0.131$, $C_{11/6} = 2^{-7/3}(\sqrt{3} - 1)\pi^{13/6}\Gamma(-11/6) \approx 6.32$, and $C_1 = \pi^3 \approx 31.01$.

We note that $\overline{\chi'^2}$ across all regimes can be expressed in terms of the Reynolds number and two length-scale ratios. In Equation (44) we chose L/L_0 which compares propagation distance with the largest scales of the flow, and L_0/λ (or η/λ) which compares turbulent scales with the optical wavelength. The range of applicability for each expression can also be put in terms of these three governing parameters (R_{L_0} , L/L_0 , and L_0/λ). For example, the classical 11/6 range (third line in Equation (44)) is valid for $R_{L_0}^{-3/4} \ll \sqrt{(\lambda/L_0)(L/L_0)} \ll 1$.

To non-dimensionalize the transition distances listed in Table 1, one could use Kolmogorov scale η since a number of expressions can be immediately written in terms of a length scale of the form $(\eta\kappa)^q \eta$, for some q . Alternatively, if the distance is normalized by the integral length scale, that is

$$\mathcal{L} \equiv L/L_0,$$

then all Kolmogorov scales in the expressions can be written in terms of \mathcal{L} using $L/\eta = \mathcal{L}R_{L_0}^{3/4}$. The transitions so obtained are tabulated in Table 3 for $\gamma = \{1, 2\}$ and $r = 0$. These

Table 3. Normalized transition distance $\mathcal{L} = L/L_0$ for $\overline{\chi'^2}$ when $r = 0$ for $\gamma = \{1, 2\}$.

Transition	$\gamma = 1$	$\gamma = 2$
$\mathcal{L}_{4 \rightarrow 3}$	$\frac{4.24\alpha \Gamma\left(\frac{7}{3}, \frac{\alpha}{R_{L_0}^{3/4}}\right)}{R_{L_0}^{3/4}}$	$\frac{13.05\sqrt{\alpha} \Gamma\left(\frac{7}{6}, \frac{\alpha}{R_{L_0}^{3/2}}\right)}{R_{L_0}^{3/4}}$
$\mathcal{L}_{3 \rightarrow \frac{11}{6}}$	$\frac{15.32\alpha^2}{R_{L_0}^{3/2} \Gamma\left(\frac{7}{3}, \frac{\alpha}{R_{L_0}^{3/4}}\right)^{6/7}} \left(\frac{L_0}{\lambda}\right)$	$\frac{27.75\alpha}{R_{L_0}^{3/2} \Gamma\left(\frac{7}{6}, \frac{\alpha}{R_{L_0}^{3/2}}\right)^{6/7}} \left(\frac{L_0}{\lambda}\right)$
$\mathcal{L}_{\frac{11}{6} \rightarrow 1}$	$\frac{6.74\alpha \Gamma\left(-\frac{5}{6}, \frac{\alpha}{R_{L_0}^{3/2}}\right)^{6/5}}{R_{L_0}^{3/2}} \left(\frac{L_0}{\lambda}\right)$	
$\mathcal{L}_{4 \rightarrow \frac{11}{6}}$	$\frac{8.47\alpha^{20/13}}{R_{L_0}^{15/13}} \left(\frac{L_0}{\lambda}\right)^{7/13}$	$\frac{19.59\alpha^{10/13}}{R_{L_0}^{15/13}} \left(\frac{L_0}{\lambda}\right)^{7/13}$
$\mathcal{L}_{4 \rightarrow 1}$	$\frac{7.95\alpha^{25/18} \sqrt[3]{\Gamma\left(-\frac{5}{6}, \frac{\alpha}{R_{L_0}^{3/2}}\right)}}{R_{L_0}^{5/4}} \left(\frac{L_0}{\lambda}\right)^{2/3}$	$\frac{14.57\alpha^{5/6} \sqrt[3]{\Gamma\left(-\frac{5}{6}, \frac{\alpha}{R_{L_0}^{3/2}}\right)}}{R_{L_0}^{5/4}} \left(\frac{L_0}{\lambda}\right)^{2/3}$
$\mathcal{L}_{3 \rightarrow 1}$	$\frac{10.88\alpha^{19/12} \sqrt{\Gamma\left(-\frac{5}{6}, \frac{\alpha}{R_{L_0}^{3/2}}\right)}}{R_{L_0}^{3/2} \sqrt{\Gamma\left(\frac{7}{3}, \frac{\alpha}{R_{L_0}^{3/4}}\right)}} \left(\frac{L_0}{\lambda}\right)$	$\frac{15.39\alpha \sqrt{\Gamma\left(-\frac{5}{6}, \frac{\alpha}{R_{L_0}^{3/2}}\right)}}{R_{L_0}^{3/2} \sqrt{\Gamma\left(\frac{7}{6}, \frac{\alpha}{R_{L_0}^{3/2}}\right)}} \left(\frac{L_0}{\lambda}\right)$

Table 4. Normalized transition distance $\mathcal{L} = L/L_0$ (same as Table 3) in the limit $R_{L_0} \rightarrow \infty$ for $\overline{\chi^2}$.

Transition	$\gamma = 1$	$\gamma = 2$
$\mathcal{L}_{4 \rightarrow 3}$	$\frac{5.04\alpha}{R_{L_0}^{3/4}}$	$\frac{12.11\sqrt{\alpha}}{R_{L_0}^{3/4}}$
$\mathcal{L}_{3 \rightarrow \frac{11}{6}}$	$\frac{13.19\alpha^2}{R_{L_0}^{3/2}} \left(\frac{L_0}{\lambda}\right)$	$\frac{29.60\alpha}{R_{L_0}^{3/2}} \left(\frac{L_0}{\lambda}\right)$
$\mathcal{L}_{\frac{11}{6} \rightarrow 1}$	$8.39 \left(\frac{L_0}{\lambda}\right)$	
$\mathcal{L}_{4 \rightarrow \frac{11}{6}}$	$\frac{8.47\alpha^{20/13}}{R_{L_0}^{15/13}} \left(\frac{L_0}{\lambda}\right)^{7/13}$	$\frac{19.59\alpha^{10/13}}{R_{L_0}^{15/13}} \left(\frac{L_0}{\lambda}\right)^{7/13}$
$\mathcal{L}_{4 \rightarrow 1}$	$\frac{8.45\alpha^{10/9}}{R_{L_0}^{5/6}} \left(\frac{L_0}{\lambda}\right)^{2/3}$	$\frac{15.48\alpha^{5/9}}{R_{L_0}^{5/6}} \left(\frac{L_0}{\lambda}\right)^{2/3}$
$\mathcal{L}_{3 \rightarrow 1}$	$\frac{10.93\alpha^{7/6}}{R_{L_0}^{7/8}} \left(\frac{L_0}{\lambda}\right)$	$\frac{17.50\alpha^{7/12}}{R_{L_0}^{7/8}} \left(\frac{L_0}{\lambda}\right)$

transitions are a function of the small-scale parameter α , Reynolds number and the normalized optical wavelength L_0/λ . In the high-Reynolds number limit, that is $R_{L_0} \rightarrow \infty$ expressions are simplified significantly as seen in Table 4.

It is interesting to observe that in the limit of infinite Reynolds number, the only non-zero transition is $\mathcal{L}_{\frac{11}{6} \rightarrow 1}$. This would imply that $\overline{\chi^2}$ scales as $\mathcal{L}^{11/6}$ from the source and then transitions to a linear scaling at a normalized distance that is independent of the Reynolds number given by $\mathcal{L}_{\frac{11}{6} \rightarrow 1} = 8.39(L_0/\lambda)$ from Table 4. However, we note that since the propagation distance L in this analysis is normalized by the integral scale L_0 , the limit $R_{L_0} \rightarrow \infty$ implicitly assumes a finite L_0 . Thus the normalized transitions listed in Table 4 are equivalent to the transition distance obtained in the limit $\eta \rightarrow 0$ in Table 1.

Similar to Equation (44), we can also write the different scaling regimes for the variance of fluctuations in phase as

$$\overline{S^2} = C_n^2 \rho_{\text{rms}}^2 K_{GD}^2 \begin{cases} \left(2\pi^2 \sqrt[3]{\alpha} R_{L_0}^{-1/2} \Gamma\left(-\frac{1}{3}\right) {}_1F_1\left(-\frac{1}{2}; \frac{4}{3}; -\frac{\alpha}{R_{L_0}^{3/2}}\right) \right. \\ \left. + \pi^{5/2} \Gamma\left(\frac{11}{6}\right) \Gamma\left(\frac{1}{3}\right) {}_1F_1\left(-\frac{5}{6}; \frac{2}{3}; -\frac{\alpha}{R_{L_0}^{3/2}}\right) \right) \left(\frac{L_0}{\lambda}\right)^2 \left(\frac{L}{L_0}\right)^2, & L \ll \eta \\ 2\pi^3 \alpha^{5/6} \Gamma\left(-\frac{5}{6}, \frac{\alpha}{R_{L_0}^{3/2}}\right) \left(\frac{L_0}{\lambda}\right)^2 \left(\frac{L}{L_0}\right), & \sqrt{\lambda L} \ll \eta \\ \pi^3 \alpha^{5/6} \Gamma\left(-\frac{5}{6}, \frac{\alpha}{R_{L_0}^{3/2}}\right) \left(\frac{L_0}{\lambda}\right)^2 \left(\frac{L}{L_0}\right), & \eta \ll \sqrt{\lambda L} \end{cases} \quad (45)$$

for $r = 0$. Here again the variance depends on the normalized length scales L/L_0 and L_0/λ . The normalized transition for $\overline{S^2}$ then occurs at

$$\mathcal{L}_{2 \rightarrow 1} = \frac{2\pi \sqrt{R_{L_0}} \Gamma\left(\frac{11}{6}\right) E_{11}\left(\frac{\alpha}{R_{L_0}^{3/2}}\right)}{2\sqrt[3]{\alpha} \Gamma\left(-\frac{1}{3}\right) \Gamma\left(\frac{11}{6}\right) {}_1F_1\left(-\frac{1}{2}; \frac{4}{3}; -\frac{\alpha}{R_{L_0}^{3/2}}\right) + \sqrt{\pi} \sqrt{R_{L_0}} \Gamma\left(\frac{1}{3}\right) {}_1F_1\left(-\frac{5}{6}; \frac{2}{3}; -\frac{\alpha}{R_{L_0}^{3/2}}\right)}. \quad (46)$$

It is interesting to note that in the infinite Reynolds number limit, this transition distance approaches a universal value of $2\sqrt{\pi}\Gamma(\frac{5}{6})/\Gamma(\frac{1}{3}) \approx 1.494$ (for $\gamma = 2$) independent of optical wavenumber and other turbulent characteristics, indicating that the phase variance transitions from L^2 to L^1 at a distance not too far from the integral length scale of turbulence ($L_{2 \rightarrow 1} = 1.494L_0$).

6. Numerical simulations

To assess the theoretical developments above, we consider the so-called parabolic wave propagation (or paraxial) equation,

$$\frac{\partial A}{\partial x} = \underbrace{\frac{i}{2\kappa} \left(\frac{\partial^2 A}{\partial y^2} + \frac{\partial^2 A}{\partial z^2} \right)}_{:=c_1} + \underbrace{\frac{i}{2}(n^2 - 1)\kappa A}_{:=c_2}, \quad (47)$$

where A is the complex amplitude of the electric field $E = A \exp(ikx)$ and c_2 depends upon the refractive index n and the optical wavelength κ . Equation (1) reduces to Equation (47) when $\lambda \ll \eta$ and the wave envelope varies slowly in the propagation direction such that the term $\partial^2 A / \partial x^2$ negligible in comparison to the transverse terms. The refractive index in Equation (47) is related to the density field by $n = 1 + K_{GD}(\lambda)\rho$ where K_{GD} is the Gladstone–Dale constant. As mentioned before in the previous section, the density field is taken from the Direct Numerical Simulations (DNS) of the fully compressible Navier–Stokes equations. Some of the important details of these DNS are provided in Section 5 and also summarized in Table 2. This DNS database comprises some of the most well-resolved simulations of compressible turbulence in the literature [66].

The paraxial solver is based on eighth-order finite difference schemes for the transverse Laplacian term. Close to the boundaries, we found that for the plane-wave propagation investigated here, both periodic boundary conditions as well as gradually reducing the order of the scheme such that only information from within the domain is used, give similar results. Stability analysis in the Fourier domain [72] shows that common explicit schemes for the approximation of derivative in the direction of propagation ($\partial A / \partial x$) in Equation (47) result in an unstable discretized system. Thus for numerical stability we use an implicit two-stage second-order Runge–Kutta scheme for computing derivative in the x direction. To write the discrete form of Equation (47), we first define $\tilde{A}_{N^2 \times 1} = \text{vec}(A_{N \times N})$, where $A_{N \times N}$ is the complex amplitude in the (n) th transverse plane and the $\text{vec}(\cdot)$ operator vectorizes this matrix to yield $\tilde{A}_{N^2 \times 1}$. Here N is the number of grid points in either y or z direction. Thus N^2 is the total grid points in the y – z plane and $\Delta y = \Delta z = L_{\text{box}}/N$ is the grid spacing. The transverse Laplacian can then be written as $S := (I_{N \times N} \otimes S_y) + (S_z \otimes I_{N \times N})$, where $I_{N \times N}$ is an identity matrix and S_y and S_z are $N \times N$ matrix operators that compute the second-order spatial derivative in y and z directions, respectively. Using these definitions, we can now write the semi-discrete form of Equation (47) as

$$\left. \frac{d\tilde{A}}{dx} \right|^{(n)} = c_1 S \tilde{A}^{(n)} + c_2^{(n)} \tilde{A}^{(n)} \quad (48)$$

at plane (n). The fully-discrete equation to compute the complex amplitude in the ($n + 1$)th plane is obtained in two steps. Let $f(x^{(n)}, \tilde{A}^{(n)}) := c_1 S \tilde{A}^{(n)} + c_2^{(n)} \tilde{A}^{(n)}$, then

$$\begin{aligned}
 k_1 &= \Delta x f(x^{(n)}, \tilde{A}^{(n)}) = \Delta x \left(c_1 S \tilde{A}^{(n)} + c_2^{(n)} \tilde{A}^{(n)} \right) \\
 k_2 &= \Delta x f(x^{(n+1)}, \tilde{A}^{(n)} + \frac{1}{2}(k_1 + k_2)) \\
 &= \Delta x \left(S \left(\tilde{A}^{(n)} + \frac{1}{2}(k_1 + k_2) \right) + c_2^{(n+1)} \left(\tilde{A}^{(n)} + \frac{1}{2}(k_1 + k_2) \right) \right) \\
 \tilde{A}^{(n+1)} &= \tilde{A}^{(n)} + \frac{1}{2}(k_1 + k_2). \tag{49}
 \end{aligned}$$

Here the first-stage k_1 is computed directly from $\tilde{A}^{(n)}$. However, the second-stage k_2 is implicit and thus requires solving a system of linear equations of the form $k_2 = K^{(n)} b$, where $K_{N^2 \times N^2}^{(n)}$ is a sparse matrix with complex coefficients that vary with (n) due to the implicit dependence of $c_2^{(n)}$ on the refractive index. To solve this system in parallel, we use the direct solvers in SuperLU [73]. Once k_1 and k_2 are known, the last equation in Equation (49) yields the complex amplitude in the ($n + 1$)th transverse plane.

We first performed a rigorous convergence study for log-amplitude variance ($\overline{\chi'^2}$). For that, we note that since c_2 is a function of κ , a non-dimensional parameter of the form $\kappa \Delta x$ appears in the discrete form of Equation (47) listed in Equation (49). Thus it is natural that the convergence criterion will depend on $\kappa \Delta x$, and it can be obtained by looking at the value of $\overline{\chi'^2}$ at very short propagation distance L . At this distance, $\overline{\chi'^2}$ is in the L^4 scaling regime listed in Equation (18) and therefore, independent of optical wavelength. The results of this study are shown in Figure 4 for three different optical wavelengths, $\kappa \approx 6.28 \times 10^3 \text{ m}^{-1}$ (red), $\kappa \approx 6.28 \times 10^4 \text{ m}^{-1}$ (blue), and $\kappa \approx 6.28 \times 10^5 \text{ m}^{-1}$ (magenta). For $\kappa \Delta x < 20$, the log-amplitude variance attains a constant value which is also independent of the wavelength. This indicates that, at least for the conditions analyzed in this work, $\kappa \Delta x < 20$ is the resolution criterion in the propagation direction. For larger values of $\kappa \Delta x$ (i.e. coarser grid in the direction of propagation), $\overline{\chi'^2}$ is not converged and takes value that depends upon κ even in the L^4 and L^3 regimes. We have also found that for short distances (L^4 and L^3) the resolution in transverse direction has a negligible effect on $\overline{\chi'^2}$ when $\kappa \Delta y$ (and $\kappa \Delta z$) is of order of a few hundreds. As expected the transverse resolution becomes important beyond L^3 where diffraction significantly contributes to the variance of log-amplitude.

The density field from our DNS database accurately resolves length scales up to Kolmogorov scale (η). Since these Kolmogorov scales are larger than the optical wavelength ($\lambda \ll \eta$), in the x direction we interpolate the density field (and, consequently, the refractive index), such that $\kappa \Delta x < 20$ is satisfied. Since density itself is well-resolved, we found that linear interpolation is enough to create a finer resolved field in the direction of propagation. The maximum and minimum $\kappa \Delta x$ for all the simulations presented in this work satisfy the convergence bound and are also tabulated in Table 5. Due to this strict resolution criteria, the computational cost incurred by the paraxial solver is very steep since a complex sparse system of equations of size $N^2 \times N^2$ has to be solved $L_{end}/\Delta x$ times, L_{end} being the total propagation distance, with very small increments in x ($\Delta x = 2\pi L_{rescale}/N_x < 20/\kappa$).

The log-amplitude variance for different Reynolds number and density fluctuations is shown in Figures 5 and 6 for optical wavelengths, $\lambda = 10.64 \mu\text{m}$ (or $\kappa \approx 5.91 \times 10^5 \text{ m}^{-1}$

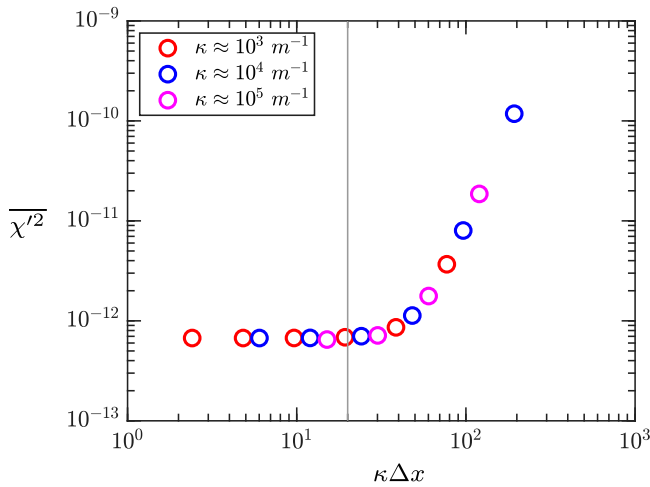


Figure 4. Variation of $\overline{\chi^2}$ with $\kappa \Delta x$ for different optical wavelengths. Colors denote optical wavelengths.

Table 5. Maximum and minimum resolution in the propagation direction ($\kappa \Delta x$) and transverse direction ($\kappa \Delta y = \kappa \Delta z$) for all the cases.

Case (R_Δ, M_t, σ)	$\{(\kappa \Delta x)_{\min}, (\kappa \Delta x)_{\max}\}$	$\{(\kappa \Delta y)_{\min}, (\kappa \Delta y)_{\max}\}$
(20, 0.3, 80%)	{0.41, 0.51}	{26.46, 264.55}
(20, 0.3, 50%)	{0.41, 0.51}	{26.46, 264.55}
(38, 0.4, 100%)	{0.85, 2.13}	{55.42, 554.24}
(60, 0.2, 30%)	{0.92, 9.23}	{59.27, 593.74}
(100, 0.3, 100%)	{1.22, 12.18}	{78.25, 784.46}
(100, 0.6, 100%)	{6.82, 17.04}	{109.47, 1094.74}
(160, 0.2, 60%)	{15.57, 15.57}	{124.81, 124.81}
(240, 0.5, 70%)	{8.56, 8.56}	{137.14, 137.14}

in red), $\lambda = 5.32 \mu\text{m}$ (or $\kappa \approx 1.18 \times 10^6 \text{ m}^{-1}$ in dark red) and $\lambda = 1.064 \mu\text{m}$ (or $\kappa \approx 5.91 \times 10^6 \text{ m}^{-1}$ in faded red). Important DNS parameters including Mach number, ratio of Kolmogorov to integral length scale are included in Table 2. An additional parameter σ in the simulations is used to control the magnitude of dilatational forcing [66, 67]. The motivation for utilizing this technique is that the magnitude of density fluctuations and, consequently, the structure-function parameter C_n^2 increase as the percentage of dilatational forcing is increased (Section 5.1). This approach can thus be exploited to span a larger parameter space of turbulence characteristics.

At very short distances, we see in Figures 5 and 6 that regardless of the turbulent flow conditions, the log-amplitude exhibits an L^4 scaling independent of the optical wavelength. This is exactly what the theoretical findings in Section 3.2.1 predict. The dashed line in faded-blue is the theoretical prediction Equation (18) for the L^4 regime with $\gamma = 1$ and an approximate α value obtained from refractive-index spectra in Figure 2(b). There is excellent agreement between the simulation data and theory especially since the latter does not rely on free fitting parameters since C_n^2 , α , and γ are obtained from structure functions for the refractive index and its spectrum, respectively. The gray-dashed vertical line is the

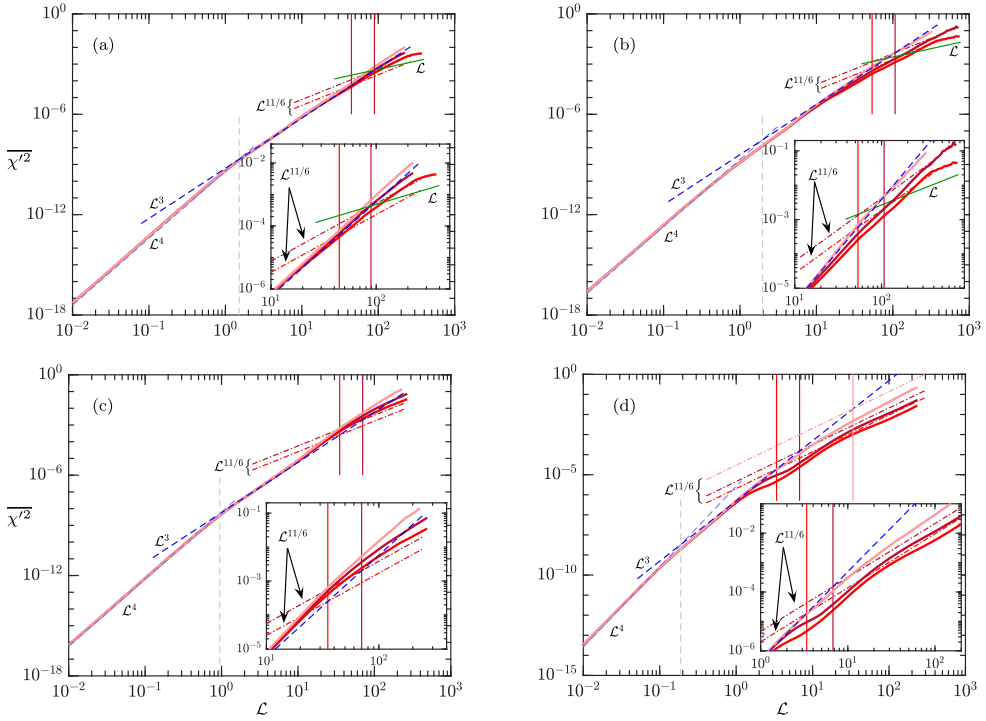


Figure 5. Evolution of $\overline{\chi^2}$ plotted against normalized propagation distance $\mathcal{L} = L/L_0$ for cases 1–4 ((a) to (d)) tabulated in Table 2. Solid lines are different optical wavelengths: $\kappa \approx 5.91 \times 10^5 \text{m}^{-1}$ (red), $\kappa \approx 1.18 \times 10^6 \text{m}^{-1}$ (dark red), $\kappa \approx 5.91 \times 10^5 \text{m}^{-1}$.

theoretical transition from L^4 to L^3 , that is Equation (35), which is seen to agree well with the transition observed in the simulations. At a distance beyond this transition point, the log-amplitude variance grows as L^3 and is in very close superposition with the dashed-blue line that corresponds to the theoretical expression given by Equation (19). It is important to note here that both L^4 and L^3 regimes are sensitive to the small-scale characteristics of turbulence (γ, α and η), with the former being more so, as Equation (18) presents a stronger dependence on α than the L^3 regime. Thus to capture the scaling of variance in log-amplitude fluctuations at short distances, the parameters characterizing the small-scales of turbulence need to be estimated accurately.

When the propagation distance is further increased such that the parameter $\sqrt{\lambda L}$ is comparable to or larger than the Kolmogorov scale (but still smaller than the integral length scale), the log-amplitude variance deviates from L^3 scaling as transition to the $L^{11/6}$ regime is initiated. The solid vertical line in Figures 5 and 6 depicts the theoretical transitions in Equation (36) with color of the line corresponding to the optical wavelength. This transition to $L^{11/6}$, which also depends upon κ , is seen to agree with the numerical data. However, we also see that the transition to $L^{11/6}$ is rather stretched, which is also consistent with the findings in Section 3.2.3 when $\gamma \neq 2$ (Figure 1a). Looking closely in the insets in Figure 5 (zoom-in on the variance at large L), we note that the departure from L^3 occurs at a shorter distance for smaller optical wavenumber, also consistent with theory and the value of $\overline{\chi^2}$

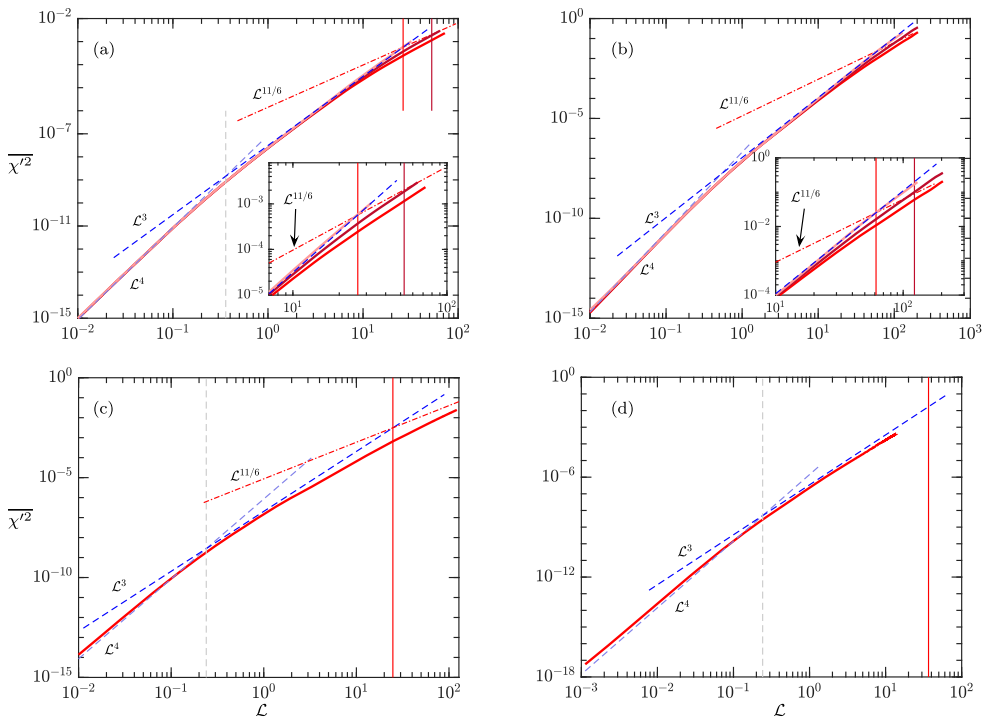


Figure 6. Evolution of $\overline{\chi^2}$ plotted against normalized propagation distance $\mathcal{L} = L/L_0$ for cases 5–8 ((a) to (d)) tabulated in Table 2. Solid lines are different optical wavelengths: $\kappa \approx 5.91 \times 10^5 m^{-1}$ (red), $\kappa \approx 1.18 \times 10^6 m^{-1}$ (dark red), $\kappa \approx 5.91 \times 10^5 m^{-1}$.

itself depends on κ . For the case $(R_\Lambda, M_t, \sigma) = (20, 0.3, 80\%)$ with no distinct inertial range, a clear $L^{11/6}$ scaling is not observed for $\lambda = 10.64 \mu m$. However, we do see that $\overline{\chi^2}$ eventually scales linearly with propagation distance as in Equation (24) which is depicted as the green line. This particular case is also shown in Figure 7(b) (to be discussed below) as the black-vertical line that goes through all the four scaling regime for the log-amplitude variance. At higher levels of dilatational forcing, for example, when $(R_\Lambda, M_t, \sigma) = (20, 0.3, 50\%)$, the $L^{11/6}$ regime is very apparent and is also in excellent agreement with the theoretical expression from Equation (23) represented in dashed-dotted lines with color corresponding to the value of κ .

The case in Figure 5(c,d) which corresponds respectively to cases $(R_\Lambda, M_t, \sigma) = (38, 0.4, 100\%)$ and $(60, 0.2, 30\%)$, show a similar general agreement with theory. However, we also see that in (d), the transition from L^3 to $L^{11/6}$ starts at a distance predicted accurately by Equation (36), though the transition seems to be long and presents some undulations. We found that this is, in part, due to the highly dilatational content of this flow, which also present higher statistical variability. It is interesting to note that the theoretical results are based on a K41 spectrum which is clearly not seen for the refractive index in this case (Figure 2b). We, thus, conclude that while not all details are predicted by the theory, the classical analysis appears to be able to reproduce the main scaling regimes for the log-amplitude variance. This is also true for the high Reynolds number cases (Figure 6a–d).

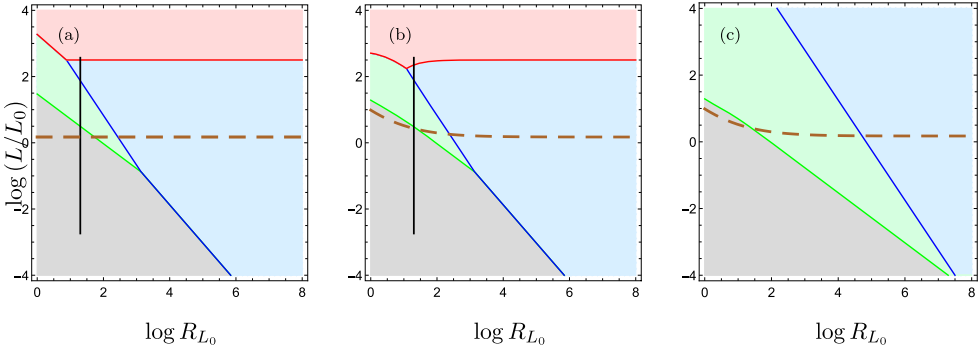


Figure 7. Scaling regimes in the R_{L_0} - \mathcal{L} plane for $L_0/\lambda = 37.8$ with (a) transitions in the limit $R_{L_0} \rightarrow \infty$ listed in Table 4 and (b) general transition distances listed in Table 3. (c) Scaling regimes obtained for $L_0/\lambda = 10^5$ and transition distances listed in Table 3. Different colors represent variance of log-amplitude fluctuations scaling as L^4 (gray), L^3 (green), $L^{11/6}$ (blue), and L (red). The dashed-brown line denotes transition of variance of fluctuations in phase from L^2 to L and the black vertical line corresponds to the DNS data for the case $(R_\Lambda, M_t, \sigma) = (20, 0.3, 80\%)$.

7. Discussion and conclusion

We presented a generalization of Tatarski's theory to quantify the distortions in the phase and amplitude of a plane wave as it encounters turbulence and thus, density (or refractive index) fluctuations, along the path. Unlike Tatarski's work [2] that assumes Kolmogorov turbulence [11], we use a more realistic representation of turbulence fluctuations (Equation 17) with intermittency correction (r) in the inertial-range scaling and the roll-off in dissipation range or high wavenumbers through γ and α . We also identify that the classical theory [2] fails to capture the variance of log-amplitude and phase fluctuations at short distances. In particular, we show that at propagation distance (L) of the order of Kolmogorov scale (η), the log-amplitude and phase variances scale as L^4 and L^2 , respectively. These previously unknown scaling regimes are very sensitive to the parameters that characterize the small scales of turbulence. The variance of log-amplitude ($\overline{\chi'^2}$) in the L^4 regime is independent of the optical wavelength (κ), contrary to the phase variance at the same distances which scale as L^2 .

At relatively larger propagation distances that still satisfy $\sqrt{\lambda L} \ll \eta$, we have $\overline{\chi'^2} \sim L^3$. While this regime also appears in Tatarski's work, here we show that the numerical prefactor in the L^3 regime depends strongly on the turbulent field parameters (r, α, η, γ) and is also sensitive to the outer-scale of turbulence (L_0) at low Reynolds-number. On further increasing the propagation distance, we obtain the well-known $L^{11/6}$ scaling regime for the variance of log-amplitude fluctuations. However, with realistic turbulence, $\overline{\chi'^2}$ actually scales as $L^{r/4+11/6}$ with dependence on the optical wavenumber modified to $\kappa^{-r/4+7/6}$. Furthermore, for a finite outer-scale L_0 , the log-amplitude variance eventually transitions to a linear scaling (i.e. $\overline{\chi'^2} \sim L$) at a finite propagation distance. In the classical work, these effects related to finite outer scales are also not considered. We further found that it is only for finite outer-scale of turbulence that one can obtain theoretical scaling laws for the variance of phase fluctuations ($\overline{S'^2}$).

The theoretical expressions for variance of both phase and log-amplitude depend on length scales that characterize the turbulent field as well as the optical wavelength.

Another *dimensional* parameter that appears in these variances, irrespective of the regime, is the refractive-index structure-function parameter C_n^2 . To ease comparison across different experiments, models and, theoretical works, we define $C_n'^2$, a normalized version of the structure parameter, which appears to be an appropriate universal constant of $\mathcal{O}(1)$. With this $C_n'^2$ and the ratio of smallest and largest scales of turbulence expressed in terms of Reynolds number R_{L_0} , we can then write universal functions $\overline{\chi'^2} = \overline{\chi'^2}(\mathcal{L}, L_0/\lambda, R_{L_0})$ and $\overline{S'^2} = \overline{S'^2}(\mathcal{L}, L_0/\lambda, R_{L_0})$ where, as before, $\mathcal{L} \equiv L/L_0$. This non-dimensionalization allows us to concisely present all the scaling regimes in a R_{L_0} vs. \mathcal{L} plane for different values of L_0/λ .

An example is shown in Figure 7(a–c) where different shaded regions represent different regimes of log-amplitude variance and the dashed-brown line indicates the transition from L^2 (below the line) to L regime (above the line) for the phase variance. The transitions in Figure 7(a) correspond to the limit $R_{L_0} \rightarrow \infty$ listed in Table 4 with $L_0/\lambda \approx 37.8$. The black vertical line overlaying on the R_{L_0} - \mathcal{L} phase plane in Figure 7(a,b) denotes the simulation data for the case $(R_\Lambda, M_t, \sigma) = (20, 0.3, 80\%)$ shown in Figure 5(a) in red ($L_0/\lambda \approx 37.8$). From Figure 7(a), we may be tempted to conclude that one would barely see a linear scaling regime for the variance of the log-amplitude towards the end of the propagation in the simulation. However, Figure 5(a) shows a very clear linear scaling for $\overline{\chi'^2}$. The reason for this difference stems from the fact that Figure 7(a) was based on an unbounded outer-scale for the turbulence. If instead, we use the general expressions listed in Table 3 with finite length-scales of turbulence, we obtain the R_{L_0} - \mathcal{L} phase plane in Figure 7(b).

There are significant differences between Figure 7(a,b) at low Reynolds number in the scaling regimes for both log-amplitude and phase. We can now see that the simulation data (black line in Figure 7b) extends considerably into the linear regime as is also observed in Figure 5(a) and its extent in the $L^{11/6}$ regime itself (blue region) is rather shortened in comparison to Figure 7(a). Lastly in Figure 7(c), we show the R_{L_0} - \mathcal{L} phase plane with $L_0/\lambda = 10^5$. This large value of L_0/λ corresponds to an electromagnetic wave of optical wavelength $\lambda = 1\mu\text{m}$ traversing through a turbulent region with outer scale L_0 of the order of 10 cm. We can see that under these conditions, that are typically expected at laboratory scales, the transition to the $L^{11/6}$ is pushed to very large propagation distances, often longer than the entire length of the experimental set-up. The R_{L_0} - \mathcal{L} phase plane presented here can help assess expected scaling regimes for a wide range of conditions and can be extremely useful in experimental design. This is critical if theoretical results in specific regimes will be used to estimate, e.g. C_n^2 . In an experimental setup with a large-scale Reynolds number of a few thousands and $L_0 \approx 10$ cm, the transition to $L^{11/6}$ could happen at distances of a few hundred meters. This kind of assessment based on the R_{L_0} - \mathcal{L} plane can also be useful in predicting the different scaling regimes anticipated in atmospheric turbulence where the Reynolds number itself varies with the time of the day.

To verify the theoretical results developed in this work and systematically assess all the scaling regimes for variance of log-amplitude and phases, we developed a paraxial solver. This solver uses explicit schemes to approximate spatial derivatives in the transverse plane and an implicit scheme for propagating the solution forward in space. The density fluctuations are taken directly from some of the best-resolved direct numerical simulations of compressible Navier–Stokes equations in the literature. Detailed convergence studies show that to obtain grid convergence for the variance of log-amplitude fluctuations, a very small discretization step that satisfies $\kappa \Delta x \leq 20$ is required. This small-scale resolution criterion together with the implicit nature of the solver which relies on linear-algebra packages

(e.g. superLU) to solve the resulting massive linear system of equations in parallel, make the paraxial solver computationally expensive. We presented the scaling of $\chi^{1/2}$ with propagation distance for a wide range of turbulent conditions. The new L^4 regime predicted by theory was confirmed by the simulation data. The L^3 , $L^{11/6}$, and L^1 regimes were also observed in the simulations with a good agreement with the corresponding theoretical expressions. Despite some small statistical differences, especially at high levels of dilational forcing, the theoretical analysis predicts all the scaling regimes for the log-amplitude variance. This may be the first and most comprehensive validation of classical theory using highly-resolved direct numerical simulations.

We close by noting future extensions of this work. First it would be important to further develop the massively parallel paraxial solver at even larger scales, so that distortions in both phase and amplitude at very large propagation distances and for a wider range of optical wavelengths can be investigated in detail. This will also be necessary to perform simulations at much higher Reynolds number found in the literature. While the transverse resolution, as we show here, does not play a significant role at short distance, its effect when diffraction becomes important at large distances needs to be systematically investigated. This also requires alternate boundary treatments such as absorption boundary condition and prematched boundary layer [74–78]. Our on-going efforts also show that the variance of phase is particularly challenging because of the added complexity involved with unwrapping of the phases. This will be discussed in detail elsewhere. The systematic investigation of the effect of Reynolds number, Mach number as well as forcing is also part of our future work. Interestingly, the good agreement between simulations and theoretical findings also suggests that some of the details missed by the spectral model used in this work, may not strongly influence some aspects of laser propagation, at least to some of the second-order statistics presented here. This requires further investigation.

We are also exploring the effect of anisotropic turbulence on phase and log-amplitude variances, specifically at short distances where we discovered new scaling regimes. Several studies [39, 53, 79] show that anisotropy only affects the prefactor in scaling laws for different measures of optical distortions while leaving the actual power-law unaltered. Similar effects can be expected at short propagation distances as well. In addition to the variance, we are also interested in the higher-order moments of both phase and log-amplitude that provide deeper insights into the small scale structures and intense features.

Acknowledgments

The views and conclusions contained in this document are those of the authors and should not be interpreted as representing the official policies, either expressed or implied, of the Army Research Office or the U.S. Government. The U.S. Government is authorized to reproduce and distribute reprints for Government purposes notwithstanding any copyright notation herein. The authors gratefully acknowledge support from the Extreme Science and Engineering Discovery Environment (XSEDE) for computational resources. The authors also benefited from extensive and enlightening discussions with Drs. Richard Miles, Christopher Limbach, James Creel, and Albina Tropina.

Disclosure statement

No potential conflict of interest was reported by the author(s).

Funding

Research was sponsored by the Army Research Office and was accomplished under Cooperative Agreement Number W911NF-19-2-0243.

References

- [1] Tyson R. Principles of adaptive optics. 3rd. Boca Raton, FL: CRC Press; 2010.
- [2] Tatarski VI. Wave propagation in a turbulent medium. Mineola, NY: Dover Publications; 2016.
- [3] Sutton GW. Effect of turbulent fluctuations in an optically active fluid medium. *AIAA J.* 1969;7(9):1737–1743.
- [4] Truman CR, Lee MJ. Effects of organized turbulence structures on the phase distortion in a coherent optical beam propagating through a turbulent shear flow. *Phys Fluids.* 1990;2(5):851–857.
- [5] Truman C. The influence of turbulent structure on optical phase distortion through turbulent shear flows. In: Annual interceptor technology conference; Huntsville, AL, USA. American Institute of Aeronautics and Astronautics; 1992.
- [6] Jumper EJ, Fitzgerald EJ. Recent advances in aero-optics. *Prog Aerosp Sci.* 2001;37(3):299–339.
- [7] Siegenthaler J, Gordeyev S, Jumper E. Shear layers and aperture effects for aero-optics. In: 36th AIAA plasmadynamics and lasers conference; Toronto, Ontario, Canada. American Institute of Aeronautics and Astronautics; 2005.
- [8] Gao Q, Jiang Z, Yi S, et al. Optical path difference of the supersonic mixing layer. *Appl Opt.* 2010;49(19):3786.
- [9] Wang M, Mani A, Gordeyev S. Physics and computation of aero-optics. *Annu Rev Fluid Mech.* 2012;44(1):299–321.
- [10] Farrell TC. The effect of atmospheric optical turbulence on laser communication systems: Part 2, practice. In: Chen G, Pham KD, editors. Sensors and systems for space applications XII; Vol. 11017; International Society for Optics and Photonics. SPIE; 2019. p. 100–116. DOI:10.1117/12.2520059.
- [11] Kolmogorov AN. Local structure of turbulence in an incompressible fluid for very large Reynolds numbers. *Dokl Akad Nauk SSSR.* 1941;30:299–303.
- [12] McGlamery BL. Computer simulation studies of compensation of turbulence degraded images. In: Urbach JC, editor. Image processing; Vol. 0074; International Society for Optics and Photonics. SPIE; 1976. p. 225–233. DOI:10.1117/12.954724.
- [13] Johansson EM, Gavel DT. Simulation of stellar speckle imaging. In: Breckinridge JB, editor. Amplitude and intensity spatial interferometry II; Vol. 2200; International Society for Optics and Photonics. SPIE; 1994. p. 372–383. DOI:10.1117/12.177254.
- [14] Sedmak G. Implementation of fast-fourier-transform-based simulations of extra-large atmospheric phase and scintillation screens. *Appl Opt.* 2004;43(23):4527–4538.
- [15] Jimenez DAL, Kumar V, Gudimetla VSR. Characterization of laser propagation over a long path through atmospheric turbulence. In: Dubinskiy M, Newell TC, editors. Laser technology for defense and security XIV; Vol. 10637; International Society for Optics and Photonics. SPIE; 2018. p. 135–143. DOI:10.1117/12.2305212.
- [16] Andrews L, Phillips R, Hopen C. Laser beam scintillation with applications. Society of Photo Optical; 2001. Online access with subscription: SPIE Digital Library. Available at <https://books.google.com/books?id=f8Kf4I88T04C>.
- [17] Gracheva ME, Gurvich A. Strong fluctuations in the intensity of light propagated through the atmosphere close to the earth. *Sov Radiophys.* 1965;8:511–515.
- [18] Andrews LC, Al-Habash MA, Hopen CY, et al. Theory of optical scintillation: Gaussian-beam wave model. *Waves Random Med.* 2001;11(3):271–291.
- [19] Vetelino FS, Young C, Andrews L, et al. Scintillation: theory vs. experiment. In: Young CY, Gilbreath GC, editors. Atmospheric propagation II; Vol. 5793; International Society for Optics and Photonics. SPIE; 2005. p. 166–177. DOI:10.1117/12.603992.
- [20] Gracheva ME, Gurvich AS, Kashkarov SS, et al. Similarity relations and their experimental verification for strong intensity fluctuations of laser radiation. In: Amelinkcx S, Chebotayev VP, Gomer R,

- et al., editors. Laser beam propagation in the atmosphere. Vol. 25. Berlin, Heidelberg: Springer; 1978. p. 107–127.
- [21] Consortini A, Churnside JH, Hill RJ, et al. Inner-scale effect on irradiance variance measured for weak-to-strong atmospheric scintillation. *J Opt Soc Am.* 1993;10(11):2354.
- [22] Clifford SF, Ochs GR, Lawrence RS. Saturation of optical scintillation by strong turbulence. *J Opt Soc Am.* 1974;64(2):148.
- [23] Hill RJ, Clifford SF. Theory of saturation of optical scintillation by strong turbulence for arbitrary refractive-index spectra. *J Opt Soc Am.* 1981;71(6):675.
- [24] Hill RJ. Theory of saturation of optical scintillation by strong turbulence: plane-wave variance and covariance and spherical-wave covariance. *J Opt Soc Am.* 1982;72(2):212.
- [25] Livingston PM. Proposed method of inner scale measurement in a turbulent atmosphere. *Appl Opt.* 1972;11(3):684.
- [26] Hill RJ, Clifford SF. Modified spectrum of atmospheric temperature fluctuations and its application to optical propagation. *J Opt Soc Am.* 1978;68(7):892.
- [27] Andrews L. An analytical model for the refractive index power spectrum and its application to optical scintillations in the atmosphere. *J Mod Opt.* 1992;39(9):1849–1853. DOI:10.1080/09500349214551931 .
- [28] Wolfe WL, Zizis GJ. The infrared handbook. Environmental Research Institute of Michigan; 1978. (IRIA series in infrared & electro-optics).
- [29] Edlén B. The refractive index of air. *Metrologia.* 1966;2(2):71–80.
- [30] Monin AS, Yaglom AM. Statistical fluid mechanics. Vol. II. Cambridge, MA: MIT Press. 1975.
- [31] Andrews LC, Phillips RL, Hopen CY, et al. Theory of optical scintillation. *J Opt Soc Am.* 1999;16(6):1417.
- [32] Erickson G, Koelling F, Miles RB, et al. Laser scintillation measurements in a controlled turbulent environment. AIAA SciTech Forum and Exposition. 2021.
- [33] Kummer E. De integralibus quibusdam definitis et seriebus infinitis. *J Reine Angew Math.* 1837;1837(17):228–242 DOI:10.1515/crll.1837.17.228 .
- [34] Abramowitz M, Stegun IA. Handbook of mathematical functions, with formulas, graphs, and mathematical tables. USA: Dover Publications, Inc.. 1974
- [35] Kolmogorov AN. A refinement of previous hypotheses concerning the local structure of turbulence in a viscous incompressible fluid at high Reynolds number. *J Fluid Mech.* 1962;13:82–85.
- [36] Sreenivasan KR, Antonia RA. The phenomenology of small-scale turbulence. *Annu Rev Fluid Mech.* 1997;29:435–472.
- [37] Frisch U. Turbulence. New York, NY: Cambridge University Press; 1995.
- [38] Khurshid S, Donzis DA, Sreenivasan KR. Energy spectrum in the dissipation range. *Phys Rev Fluids.* 2018;3:Article ID 082601. DOI:10.1103/PhysRevFluids.3.082601 .
- [39] Kon AI. Qualitative theory of amplitude and phase fluctuations in a medium with anisotropic turbulent irregularities. *Waves Random Med.* 1994;4(3):297–306. DOI:10.1088/0959-7174/4/3/005 .
- [40] Stribling BE, Welsh BM, Roggemann MC. Optical propagation in non-Kolmogorov atmospheric turbulence. In: Dainty JC, editor. Atmospheric propagation and remote sensing IV; Vol. 2471; International Society for Optics and Photonics. SPIE; 1995. p. 181–196. DOI:10.1117/12.211927 .
- [41] Hamlington PE, Oran ES. Signatures of turbulence in atmospheric laser propagation. In: Gilbreath GC, Hawley CT, editors. Active and passive signatures; Vol. 7687; International Society for Optics and Photonics. SPIE; 2010. p. 175–186.
- [42] Buaria D, Sreenivasan KR. Dissipation range of the energy spectrum in high Reynolds number turbulence. *Phys Rev Fluids.* 2020;5:Article ID 092601 .
- [43] Donzis DA, Jagannathan S. Fluctuations of thermodynamic variables in stationary compressible turbulence. *J Fluid Mech.* 2013;733:221–244.
- [44] Warhaft Z. Passive scalars in turbulent flows. *Annu Rev Fluid Mech.* 2000;32:203–240.
- [45] Jagannathan S, Donzis DA. Reynolds and Mach number scaling in solenoidally-forced compressible turbulence using high-resolution direct numerical simulations. *J Fluid Mech.* 2016;789:669–707.
- [46] Donzis DA, Sreenivasan KR, Yeung PK. The Batchelor spectrum for mixing of passive scalars in isotropic turbulence. *Flow Turbul Combust.* 2010;85:549–566.

- [47] Kraichnan RH. Small-scale structure of a scalar field convected by turbulence. *Phys Fluids*. 1968;11:945–953.
- [48] Kraichnan RH. Convection of a passive scalar by a quasi-uniform random straining field. *J Fluid Mech*. 1974;64:737–762.
- [49] Batchelor GK. Small-scale variation of convected quantities like temperature in turbulent fluid. 1. General discussion and the case of small conductivity. *J Fluid Mech*. 1959;5:113–133.
- [50] Bataille F, Zhou Y. Nature of the energy transfer process in compressible turbulence. *Phys Rev E*. 1999 May;59:5417–5426. DOI:10.1103/PhysRevE.59.5417.
- [51] Aluie H, Li S, Li H. Conservative cascade of kinetic energy in compressible turbulence. *Astrophys J Lett*. 2012;751(2):L29.
- [52] John JP, Donzis DA, Sreenivasan KR. Does dissipative anomaly hold for compressible turbulence? *J Fluid Mech*. 2021;920. DOI:10.1017/jfm.2021.443.
- [53] Cui L, Xue B, Zhou F. Generalized anisotropic turbulence spectra and applications in the optical waves' propagation through anisotropic turbulence. *Opt Express*. 2015 Nov;23(23):30088–30103.
- [54] Donzis DA, Sreenivasan KR. The bottleneck effect and the Kolmogorov constant in isotropic turbulence. *J Fluid Mech*. 2010;657:171–188.
- [55] Mathews ER, Wang K, Wang M, et al. A spectral description of aero-optical phase distortions and the effects of turbulent flow scales. In: 48th AIAA plasmadynamics and lasers conference; Denver, Colorado. American Institute of Aeronautics and Astronautics; 2017.
- [56] Wheelon AD. *Electromagnetic scintillation*. Vol. 1. New York, NY: Cambridge University Press; 2001.
- [57] Phillips RL, Andrews LC. Measured statistics of laser-light scattering in atmospheric turbulence. *J Opt Soc Am*. 1981;71(12):1440–1445.
- [58] DiComo G, Helle M, Peñano J, et al. Implementation of a long range, distributed-volume, continuously variable turbulence generator. *Appl Opt*. 2016;55(19):5192.
- [59] Lawrence RS, Ochs GR, Clifford SF. Measurements of atmospheric turbulence relevant to optical propagation. *J Opt Soc Am*. 1970;60(6):826.
- [60] Dhruva B, Tsuji Y, Sreenivasan KR. Transverse structure functions in high-Reynolds-number turbulence. *Phys Rev E*. 1997;56:R4928–R4930.
- [61] Gotoh T, Fukayama D, Nakano T. Velocity field statistics in homogeneous steady turbulence obtained using a high-resolution direct numerical simulation. *Phys Fluids*. 2002;14(3):1065–1081.
- [62] Antonia RA, Burattini P. Approach to the 4/5 law in homogeneous isotropic turbulence. *J Fluid Mech*. 2006;550:175–184.
- [63] Watanabe T, Gotoh T. Inertial-range intermittency and accuracy of direct numerical simulation for turbulence and passive scalar turbulence. *J Fluid Mech*. 2007;590:117–146.
- [64] Yakhot V, Donzis DA. Anomalous exponents in strong turbulence. *Physica D*. 2018;384–385:12–17.
- [65] Sawford BL, Yeung PK. Kolmogorov similarity scaling for one-particle Lagrangian statistics. *Phys Fluids*. 2011;23:Article ID 091704.
- [66] Donzis DA, John JP. Universality and scaling in homogeneous compressible turbulence. *Phys Rev Fluids*. 2020;5:Article ID 084609.
- [67] Kida S, Orszag SA. Energy and spectral dynamics in forced compressible turbulence. *J Sci Comput*. 1990;5:85–125.
- [68] Schmidt W, Federrath C, Hupp M, et al. Numerical simulations of compressively driven interstellar turbulence. *Astron Astrophys*. 2009;494(1):127–145.
- [69] Sreenivasan KR. On the universality of the Kolmogorov constant. *Phys Fluids*. 1995;7(11):2778–2784.
- [70] Kaneda Y, Ishihara T, Yokokawa M, et al. Energy dissipation rate and energy spectrum in high resolution direct numerical simulations of turbulence in a periodic box. *Phys Fluids*. 2003;15(2):L21–L24.

- [71] Siegenthaler J, Jumper E, Gordeyev S. Atmospheric propagation vs. aero-optics. In: 46th AIAA aerospace sciences meeting and exhibit; Reno, Nevada. American Institute of Aeronautics and Astronautics; 2008.
- [72] Hirsch C. Numerical computation of internal and external flows. Vol. 1. New York. Wiley. 1994
- [73] Li XS, Demmel JW. SuperLU_DIST: a scalable distributed-memory sparse direct solver for unsymmetric linear systems. *ACM Trans Math Softw.* 2003;29(2):110–140.
- [74] Lindman E. 'Free-space' boundary conditions for the time dependent wave equation. *J Comput Phys.* 1975;18(1):66–78.
- [75] Engquist B, Majda A. Absorbing boundary conditions for the numerical simulation of waves. *Math Comput.* 1977;31:629–651.
- [76] Berenger JP. A perfectly matched layer for the absorption of electromagnetic waves. *J Comput Phys.* 1994;114(2):185–200.
- [77] Clayton R, Engquist B. Absorbing boundary conditions for acoustic and elastic wave equations. *Bull Seismol Soc Am.* 1977;67(6):1529–1540.
- [78] Vassallo C, Collino F. Highly efficient absorbing boundary conditions for the beam propagation method. *J Lightw Technol.* 1996;14(6):1570–1577.
- [79] Gudimetla VSR, Holmes RB, Riker JF. Analytical expressions for the log-amplitude correlation function for plane wave propagation in anisotropic non-Kolmogorov refractive turbulence. *J Opt Soc Am A.* 2012 Dec;29(12):2622–2627.